WFPC2 LRF imaging of emission-line nebulae in 3CR radio galaxies

Article (Published Version)

The Astrophysical Journal Supplement Series, 175:423–461, 2008 April

WFPC2 LRF IMAGING OF EMISSION-LINE NEBULAE IN 3CR RADIO GALAXIES[1]

G. C. Privon,[2] C. P. O'Dea,[3] S. A. Baum,[2] D. J. Axon,[3] P. Kharb,[2] C. L. Buchanan,[3]
W. Sparks,[4] and M. Chiaberge[4]

Received 2006 December 21; accepted 2007 October 10

ABSTRACT

We present *Hubble Space Telescope* WFPC2 Linear Ramp Filter images of high surface brightness emission lines (either [O II], [O III], or Hα + [N II]) in 80 3CR radio sources. We overlay the emission-line images on high-resolution VLA radio images (eight of which are new reductions of archival data) in order to examine the spatial relationship between the optical and radio emission. We confirm that the radio and optical emission-line structures are consistent with weak alignment at low redshift ($z < 0.6$) except in the compact steep-spectrum (CSS) radio galaxies where both the radio source and the emission-line nebulae are on galactic scales and strong alignment is seen at all redshifts. There are weak trends for the aligned emission-line nebulae to be more luminous and for the emission-line nebula size to increase with redshift and/or radio power. The combination of these results suggests that there is a limited but real capacity for the radio source to influence the properties of the emission-line nebulae at these low redshifts ($z < 0.6$). Our results are consistent with previous suggestions that both mechanical and radiant energy are responsible for generating alignment between the radio source and emission-line gas.

Subject headings: galaxies: active — quasars: emission lines — radio continuum: galaxies

1. INTRODUCTION

Radio galaxies are an important class of extragalactic objects: they represent one of the most energetic astrophysical phenomena; they may be used as probes of their environments; and they are unique probes of the early universe (McCarthy 1993). As the 3CR sample of radio galaxies is radio flux-density selected (Bennett 1962), it provides an unbiased optical sample to study the host galaxies of these radio-loud active galactic nuclei (AGNs). The sample has been well studied at multiple wavelengths and previous ground-based studies have investigated the spatial coincidence of optical emission nebulae and the radio source (Baum et al. 1988; Baum & Heckman 1989a; McCarthy et al. 1987; Chambers et al. 1987).

Chambers et al. (1987) and McCarthy et al. (1987) first demonstrated the "alignment effect" at high redshift ($z \geq 0.6$) where the continuum optical and/or infrared (IR) emission is aligned along the radio axis. An "alignment effect" for emission-line gas was also shown by McCarthy et al. (1987, 1995). In this paper we focus on the alignment of the fine-scale high surface brightness emission-line gas imaged by the *Hubble Space Telescope* (*HST*) with the radio emission. The primary mechanisms for the emission-line gas alignment are thought to be shocks induced by the radio jet and photoionization from the central AGN (e.g., Baum & Heckman 1989a; McCarthy 1993; Best et al. 2000).

McCarthy & van Breugel (1989) demonstrated the redshift dependence of the alignment effect: at $z < 0.1$ there is no alignment, at $0.1 < z < 0.6$ some alignment is seen, and for $z > 0.6$ essentially all the powerful radio galaxies show strong alignment. Baum & Heckman (1989b) found alignment at low z if one compares the emission in the quadrants containing the radio source to quadrants without radio emission. Studies which attempt to break the redshift-radio power degeneracy suggest that the alignment depends on both redshift and radio power (e.g., Inskip et al. 2002b, 2005). Thus, the alignment depends on both the presence of extended gas in the environment as well as the ability of the radio source to influence its environment.

In this paper we examine the relationship of the high surface brightness emission-line gas and radio emission over a wide range of redshift ($0.017 < z < 1.406$), focusing on the transition redshift range $z < 0.6$ where the alignment effect starts to turn on. Using the Wide Field and Planetary Camera 2 (WFPC2) on *HST*, we obtained images with resolutions of $0.05''$–$0.1''$, similar to or better than the synthesis imaging resolution obtained with the Very Large Array (VLA)[5] at 5 GHz in the "A" configuration. The higher resolution allows us to probe denser gas in the center of these galaxies. In addition, the tunable linear ramp filter (LRF) permits narrowband imaging of a selected spectral feature for a wide range of redshifts, enabling studies of a specified emission line for a sample such as the 3CR covering a large range of redshift.

Biretta et al. (2002) conducted an initial study using this data, and published a subset of the data. Here we expand on their analysis, presenting the complete set of detected images as well as statistical results.

The paper is organized in the following fashion. We discuss the properties of the sample in § 2. Section 3 discusses the observations made and the data reduction methods used. In § 4 we outline the analysis of the data. Section 5 contains a discussion of our sources and the results of our study. In § 6 we conclude by discussing the implications of our results. The Appendix contains notes for individual sources.

2. THE SAMPLE

Our sample is drawn from a set of 100 3CR radio galaxies selected from the *HST* 3CR imaging survey. Using earlier

[1] Based on observations made with the NASA/ESA *Hubble Space Telescope*, obtained at the Space Telescope Science Institute, which is operated by the Association of Universities for Research in Astronomy, Inc., under NASA contract NAS 05-26555. These observations are associated with program 5957.

[2] Chester F. Carlson Center for Imaging Science, Rochester Institute of Technology, Rochester, NY 14623.

[3] Department of Physics, Rochester Institute of Technology, Rochester, NY 14623.

[4] Space Telescope Science Institute, Baltimore, MD 21218.

[5] The National Radio Astronomy Observatory is a facility of the National Science Foundation operated under cooperative agreement by Associated Universities, Inc.

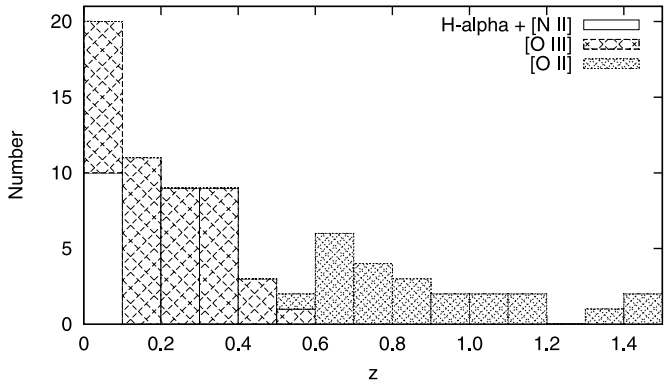

FIG. 1.—Histogram of the redshift distribution of the sources in our sample.

spectroscopic observations, objects with significant emission-line flux were selected (Biretta et al. 2002) for this study to maximize detection. Thus, our results may not be extendible to objects with very faint emission lines, and our observations do not reach uniform surface brightness in the rest frame of the object. Observations were done in the *HST* "snapshot" mode, in which targets are randomly selected from the target list for observation. There were 80 sources observed and that constitute our sample, spanning a redshift of $0.017 \leq z \leq 1.406$ (see Fig. 1). The sample contains nine Fanaroff-Riley type I (FR I) galaxies , 58 Fanaroff-Riley type II (FR II) galaxies, 12 compact steep-spectrum (CSS) sources, and one source of an unknown morphology. Of the radio galaxies, 22 have broad emission lines, while 58 have narrow emission lines in their optical spectrum.

3. OBSERVATIONS AND DATA REDUCTION

3.1. *Radio Observations*

Arcsecond-scale resolution radio maps for the sample objects were obtained from a variety of sources (referenced in figure captions). Sources for which 5 or 8 GHz VLA "A" array maps were not already available were reduced using archival data. The cleaning and self-calibration of the raw data were performed using the the NRAO AIPS software package. We present new maps for the following sources: 3C 124, 3C 135, 3C 284, 3C 303.1, 3C 341, 3C 368, 3C 379.1, and 3C 382. Table 1 lists the observation parameters for the new VLA maps, including the date of observation, frequency and rms noise of the final map.

3.2. *Optical Observations*

Snapshot images were taken using the LRFs on the *HST* WFPC2 instrument. There are three WF chips and one PC chip. The chip on which the LRF images a target varies with the selected wavelength. We have noted the chip on which a source was imaged in Table 2. Nearby objects ($z \lesssim 0.03$) were imaged in Hα + [N II]. Objects at intermediate redshifts were imaged in [O III] λ5007 and objects at high redshift ($z > 0.5$) were imaged in [O II] λ3727. Table 2 also lists which emission line was imaged for each source. All of the LRF observations consisted of a pair of 300 s exposures taken in "snapshot" mode. The images were calibrated and combined using the CRREJ procedure to remove cosmic rays (Biretta 1996). Because the design of the LRF does not allow direct observations of the flat field, the images were flat fielded using the F656N flat. Note that due to the small size of the WFPC2 pixels, we are sensitive only to high surface brightness extended emission-line gas.

TABLE 1
RADIO OBSERVATION PARAMETERS

Name	Date	Frequency (GHz)	Bandwidth (GHz)	rms Noise ($\times 10^{-4}$ Jy beam^{-1})
3C 124	1987 Aug 17	4.885	0.1	0.63
3C 135	1990 May 25	8.465	0.025	0.50
3C 284	1985 Jan 11	4.885	0.1	5.76
3C 303.1	1991 Aug 11	8.415	0.1	0.78
3C 341	1996 Dec 14	8.435	0.1	6.87
3C 368	1995 Jul 31	4.535	0.1	0.32
3C 379.1	1987 Oct 10	4.873	0.05	0.78
3C 382	1983 Sep 20	4.885	0.1	3.55

In order to obtain images of only the emission-line region (ELR), the continuum contribution to the LRF images was subtracted. This was usually done using an image of the object in the broadband F702W filter. The continuum was scaled to the observed wavelength by assuming a 3000 K blackbody spectrum for the continuum (Biretta et al. 2002). In some cases the continuum was contaminated by emission lines. Baum et al. (1988) discussed the uncertainties in flux calibration due to contamination from emission lines. Using standard line ratios, they found corrections from 1.002 to 1.36 (median 1.09). We have not applied corrections for emission-line contamination to our data, but the values given by them indicate the uncertainty due to contamination. Continuum images were not available for four sources: 3C 98, 3C 273, 3C 289, and 3C 323.1, and the subtraction could not be performed. These sources have been left out of the analysis, but their narrowband LRF images are presented if the source was detected.

4. OPTICAL DATA ANALYSIS

We grouped the emission-line nebulae into four broad optical morphological categories: "extended" sources (21 sources), "partially extended" sources (33 sources), slightly or unresolved sources (12 sources), and nondetections (11 sources). Four sources were eliminated due to the lack of a continuum image for subtraction. Sources were classified as extended if the 3 σ contour was extended compared with the expected point-spread function (PSF) in the continuum-subtracted image. Partially extended sources are those which feature extensions smaller than 2″ but do not match the PSF. They often resemble an unresolved source, with a small faint extension. We analyzed only the extended and partially extended sources, as we were able to determine reliable position angles and/or angular sizes for most of these objects. Table 3 lists the morphological categories for each object.

To examine the spatial coincidence of the ELR and the radio source, the radio and optical images for the extended sources were combined into overlays. In general, the images were registered using the radio core (for the radio sources) and the centroid of the host galaxy (obtained from the continuum images). One extended source (3C 305) has a known dust lane, making centroiding on the continuum image unreliable. We attempted to determine a center through ellipse fitting to the outer portion of the galaxy, but this was unsuccessful due to the close companion galaxy. The registration in the image presented was done using centroiding on the continuum image. The overlays are shown in Figures 10–54 along with the continuum and emission-line images for each source.

TABLE 2

Optical Observations

Source	z	M_v	WFPC2 Chip	Emission Line	Detected?	Continuum Exposure (s)
3C 6.1	0.840	...	WF2	[O II]	Yes	300
3C 17	0.219	−22.137	WF2	[O III]	Yes	2 × 140
3C 31	0.016	...	WF2	Hα, [N II]	Yes	2 × 140
3C 36	1.301	...	WF4	[O II]	Yes	300
3C 42	0.395	...	WF3	[O III]	Yes	300
3C 46	0.437	...	WF4	[O III]	Yes	300
3C 49	0.621	...	WF2	[O II]	Marginal Detection	300
3C 55	0.734	...	WF3	[O II]	No	300
3C 63	0.175	...	PC1 (F588N)	[O III]	Yes	2 × 140
3C 78	0.028	...	PC1 (F673N)	Hα, [N II]	Yes	2 × 140
3C 83.1	0.025	...	PC1 (F673N)	Hα, [N II]	Yes	2 × 140
3C 84	0.017	...	WF2	Hα, [N II]	Yes	2 × 140
3C 93	0.358	−23.247	WF2	[O III]	Yes	2 × 140
3C 93.1	0.244	−21.423	WF3	[O III]	Yes	300
3C 98	0.030	−20.155	PC1	[O III]	Yes	...
3C 103	0.330	...	WF2	[O III]	Yes	300
3C 109	0.305	−22.971	WF3	[O III]	Yes	2 × 140
3C 111	0.048	−18.564	WF3	[O III]	No	2 × 140
3C 124	1.083	...	WF4	[O II]	Yes	300
3C 135	0.127	−21.848	WF2	[O III]	Yes	2 × 140
3C 136.1	0.064	...	WF4	[O III]	Yes	2 × 140
3C 138	0.759	−24.524	PC1 (F656N)	[O II]	No	2 × 140
3C 169.1	0.633	...	WF2	[O II]	Yes	300
3C 171	0.238	−21.282	WF2	[O III]	Yes	300
3C 172	0.519	...	PC1	[O III]	Yes	300
3C 175	0.768	−26.795	PC1 (F658N)	[O II]	Yes	2 × 140
3C 184.1	0.118	−21.676	WF2	[O III]	Yes	2 × 140
3C 192	0.059	−19.980	WF3	[O III]	No	2 × 140
3C 196.1	0.198	...	WF4	[O III]	Yes	2 × 140
3C 207	0.684	−24.934	PC1 (F631N)	[O II]	Yes	2 × 140
3C 213.1	0.194	...	WF4	[O III]	Yes	300
3C 219	0.174	−22.158	PC1 (F588N)	[O III]	Yes	2 × 140
3C 220.1	0.620	...	WF2	[O II]	Yes	300
3C 223	0.136	−21.950	WF2	[O III]	Yes	2 × 140
3C 227	0.086	−21.610	WF4	[O III]	Yes	2 × 140
3C 234	0.184	−22.463	WF4	[O III]	Yes	2 × 140
3C 244.1	0.428	−23.187	WF4	[O III]	Yes	300
3C 249.1	0.311	−25.310	PC1 (F656N)	[O III]	Yes	2 × 140
3C 263	0.646	−26.612	WF2	[O II]	Yes	2 × 140
3C 264	0.020	−20.697	WF2	Hα, [N II]	Yes	2 × 140
3C 268.1	0.973	...	WF4	[O II]	No	300
3C 268.2	0.362	...	WF2	[O III]	Yes	300
3C 268.3	0.371	−21.479	WF2	[O III]	Yes	300
3C 268.4	1.400	−26.602	PC1	[O II]	No	2 × 140
3C 273	0.158	−26.516	WF3	[O III]	Yes	...
3C 277.1	0.320	−23.172	PC1	[O III]	Yes	2 × 140
3C 277.3	0.085	...	WF4	Hα, [N II]	Yes	2 × 140
3C 280	0.997	−22.101	WF3	[O II]	No	300
3C 284	0.239	...	WF2	[O III]	Yes	2 × 140
3C 289	0.967	...	WF4	[O II]	No	...
3C 297	1.406	−24.533	PC1	[O II]	Yes	300
3C 299	0.367	...	WF2	[O III]	Yes	300
3C 303.1	0.267	−22.147	WF3	[O III]	Yes	300
3C 305	0.041	−22.521	WF3	[O III]	Yes	2 × 140
3C 305.1	1.132	...	WF3	[O II]	Yes	2 × 140
3C 321	0.096	−22.194	WF3	[O III]	Yes	2 × 140
3C 323.1	0.264	−23.929	WF3	[O III]	Yes	...
3C 330	0.550	−21.504	WF3	[O II]	Yes	300
3C 332	0.151	−23.258	WF3	[O III]	Yes	2 × 140
3C 338	0.029	...	PC1 (F673N)	Hα, [N II]	Yes	2 × 140
3C 341	0.448	...	WF4	[O III]	Yes	300
3C 343.1	0.750	−22.632	WF3	[O II]	Yes	300
3C 349	0.205	...	WF2	[O III]	Yes	300
3C 352	0.805	...	PC1 (F673N)	[O II]	Yes	300
3C 356	1.079	−22.815	WF4	[O II]	No	300

TABLE 2—*Continued*

Source	z	M_v	WFPC2 Chip	Emission Line	Detected?	Continuum Exposure (s)
3C 368	1.130	...	WF3	[O II]	Yes	300
3C 379.1	0.256	...	PC1 (F631N)	[O III]	Yes	2 × 140
3C 380	0.691	−26.302	WF3	[O II]	Yes	2 × 140
3C 381	0.160	−22.157	WF3	[O III]	Yes	2 × 140
3C 382	0.058	−21.651	WF3	[O III]	Yes	2 × 140
3C 390.3	0.056	−21.582	WF3	[O III]	Yes	2 × 140
3C 402	0.025	...	PC1 (F673N)	Hα, [N II]	No	2 × 140
3C 433	0.101	−20.512	WF3	[O III]	Yes	2 × 140
3C 436	0.215	...	WF2	[O III]	Yes	2 × 140
3C 445	0.056	−21.192	WF3	[O III]	No	2 × 140
3C 449	0.017	...	WF2	Hα, [N II]	Yes	2 × 140
3C 452	0.081	−21.243	WF4	[O III]	Yes	2 × 140
3C 454.3	0.860	−27.601	PC1	[O II]	Yes	2 × 140
3C 458	0.290	...	WF3	[O III]	Yes	300
3C 465	0.029	−22.190	PC1 (F673N)	Hα, [N II]	Yes	2 × 140

NOTES.—Col. (2): Redshift of the source. Col. (3): The *V*-band host magnitude from Véron-Cetty & Véron (2003). Col. (4): WFPC2 chip on which the source was observed. When using the LRF, the chip on which a source is imaged depends on the filter's central wavelength. If the source was not imaged with the LRF, both the WFPC2 chip used and the narrow filter used are given. Col. (5): Emission line observed in the narrowband images. Col (6): If a source was detected in the narrowband images.

Position angles (PAs) for the extended sources were measured using the emission within the 3 σ contour, with the PA passing through the nucleus of the host galaxy in the direction of the longest extent of the emission-line nebulae. PAs for the partially extended sources were determined using the IRAF `ellipse` task. Radio PAs were taken from the literature (if available) or measured from hotspot-to-hotspot for FR II galaxies or across the longest extent for FR I galaxies on the radio maps. The measurement of the difference in the PAs is independent of the spatial alignment of the radio and optical images as the PAs are independently determined from the images.

A measure of alignment between the ELR and the radio source was determined by taking the absolute value of the difference in PAs of the radio source and the ELR. If $\Delta\mathrm{PA} = 30^\circ$, the ELR and radio source were considered aligned. In some cases the ELR displayed a PA for the inner regions which differed from the large-scale PA. In most cases, the usage of an "inner PA" did not cause misaligned objects to be moved into the aligned category, so only the large-scale PA was used for the purposes of our analysis.

Emission-line fluxes were measured using the IRAF `apphot` set of tasks. Luminosities and sizes were calculated using a cosmology of $H_0 = 71\,\mathrm{km\,s^{-1}}$, $\Omega_\mathrm{M} = 0.27$, and $\Omega_\mathrm{vac} = 0.73$. Values were obtained using an online cosmology calculator (Wright 2006). In order to compare the luminosities from each source, the measured fluxes were converted to Hα fluxes using line ratios derived from observations of narrow-line radio galaxies (Koski 1978). The ratios of [O III], [O II], and Hα + [N II] to Hα were 3, 1.23, and 2.08, respectively.

5. PROPERTIES OF THE NEBULAE

Here we discuss the properties of the nebulae and their relationship to the radio source. Individual source descriptions are provided in the Appendix. In Table 4 we provide morphological information about the radio structure, including classifications, PAs, and angular sizes. We also present luminosities for each source. Table 3 contains the morphological information for the continuum-subtracted emission-line images. This includes PAs, angular sizes, and fluxes. In addition, this table contains the *V*-band magnitudes for the host galaxies and the PA of the galaxy.

The detection statistics varied depending on the emission line observed. Nine of 10 sources (90%) imaged in Hα + [N II] were detected, 43 of 47 sources (91%) imaged in [O III] were detected, and 15 of 23 (65%) [O II] detections were made.

The statistical significance of the observed relationships discussed in this section are given in Table 5. The Kendall's τ value is a measure of the correlation between the specified measurements. The Spearman's ρ value is a similar measure, describing how likely the two measurements are to increase or decrease concordantly. Statistical values for noncorrelations are given in Table 6.

5.1. *Alignment Effect*

We find that 19 of 37 sources for which a PA could be measured showed alignment between the high surface brightness ELR and the radio source to within 30° (Fig. 2). We have four sources at $z > 0.6$ which all show strong alignment. In the remaining 33 sources at $z < 0.6$, 15 show alignment. The median values of the PA difference in bins of redshift do not decrease significantly as a function of z out to 0.6. However, the upper envelope of the PA differences does seem to decrease with redshift. We clearly see a weaker alignment effect at low redshift than is seen at the high redshifts $z > 0.6$. Our high-resolution *HST* data show that the lack of strong alignment at $z < 0.6$ is not due to a lack of spatial resolution.

We investigated the possibility of the misaligned objects being predominantly broad-line radio galaxies (BLRGs). According to the unified scheme (Urry & Padovani 1995), BLRGs are not expected to show alignment, as the jet would be pointing almost along the line of sight. However, BLRGs make up only 11 of the sources with measured PA differences, and several of the BLRGs show alignment (3C 234, 3C 268.3, 3C 277.1).[6] Thus, orientation of the radio jet close to the line of sight is not responsible for the misalignment at $z < 0.6$.

A potential concern is that much of the low-redshift observations ($0.03 < z < 0.5$) are obtained using the [O III] line which is higher ionization than the [O II] and Hα + [N II]. If the high-ionization gas has very different morphology and PA than the lower excitation gas, this might reduce the strength of the alignment at low redshift. However, observations of radio galaxies in

[6] 3C 268.3 and 3C 277.1 are also CSS sources.

TABLE 3

OPTICAL PROPERTIES

Source	θ (arcsec)	PA (deg)	Line Flux ($\times 10^{-15}$ ergs s^{-1} cm^{-2})	$L_{H\alpha}$ (ergs s^{-1})	θ_{cone} (deg)	Morphology	Host PA (deg)	Ref.
3C 6.1	...	...	...	...	...	Partially res.	...	
3C 17	...	41	0.35	41.2	...	Partially res.	42	2
3C 31	...	...	1.01	38.4	...	Partially res.	144	4
3C 42	...	...	0.06	41.0	...	Partially res.	153	2
3C 46	2.13	26	0.29	41.8	17	Extended	177	2
3C 83.1	...	...	...	...	...	Partially res.	166	4
3C 84	15.67	See notes	59.14	40.3	180	Extended	100	4
3C 93.1	...	65	0.35	41.3	...	Partially res.	132	2
3C 93	...	95	0.19	41.4	...	Partially res.	...	
3C 103	0.87	49	0.01	39.9	61	Partially res.	34	2
3C 109	2.34	25	1.72	42.2	39	Extended	145	1
3C 124	1.08	4	0.13	41.8	15	Extended	...	
3C 135	3.71	54	1.05	41.1	35	Extended	141	2
3C 136.1	0.53	175	0.00013	36.6	35	Partially res.	117	4
3C 169.1	...	...	0.33	41.7	...	Partially res.	...	
3C 171	3.44	85	1.38	41.8	23	Extended	165	1
3C 172	0.73	16	0.07	41.4	77	Partially res.	...	
3C 184.1	2.64	24	0.01	38.7	...	Partially res.	40	2
3C 196.1	0.67	53	0.06	40.3	15	Partially res.	57	1
3C 213.1	...	...	0.08	40.4	...	Partially res.	161	2
3C 220.1	...	...	0.06	40.9	...	Partially res.	...	
3C 223	2.1	128	2.29	41.5	43	Extended	50	1
3C 234	2.37	79	9.85	42.4	32	Extended	80	2
3C 244.1	3.47	133	0.66	42.1	25	Partially res.	76	2
3C 249.1	2.08	80	2.27	42.3	112	Extended	...	
3C 264	...	...	0.49	38.3	...	Partially res.	152	1
3C 268.2	1.8	15	0.44	41.8	56	Extended	164	2
3C 268.3	3.2	146	0.42	41.8	26	Extended	144	2
3C 277.1	1.85	124	1.4	42.1	52	Partially res.	126	3
3C 277.3	...	...	0.21	39.2	0	Partially res.	170	4
3C 284	2.9	74	0.56	41.4	30	Extended	151	2
3C 299	4.24	62	1.19	42.2	70	Extended	47	2
3C 303.1	1.56	140	0.95	41.8	38	Extended	169	2
3C 305	6.37	46	13.06	41.2	35	Extended	74	1
3C 305.1	...	33	0.05	41.4	0	Partially res.	24	3
3C 321	6.21	108	5.8	41.6	42	Extended	18	1
3C 330	1	103	0.06	40.8	47	Partially res.	...	
3C 341	1.03	172	0.27	41.8	55	Extended	17	2
3C 349	...	36	0.16	40.7	61	Partially res.	14	2
3C 352	...	8	0.05	41.1	0	Partially res.	...	
3C 368	6.74	24	0.59	42.5	24	Extended	...	
3C 379.1	0.72	43	0.06	40.6	15	Extended	...	
3C 380	...	...	0.56	42.0	0	Partially res.	131	3
3C 381	5.69	150	2.35	41.7	31	Extended	156	2
3C 382	2.14	112	13.16	41.5	49	Partially res.	85	4
3C 390.3	0	62	11.34	41.4	0	Partially res.	97	1
3C 433	5.87	135	1.49	41.1	55	Partially res.	147	1
3C 436	...	...	0.26	41.0	0	Partially res.	3	2
3C 449	1.7	174	0.37	38.0	44	Partially res.	1	4
3C 452	1.58	125	0.71	40.5	30	Partially res.	101	4
3C 454.3	...	...	0.86	42.2	...	Partially res.	...	
3C 458	...	75	0.07	40.7	...	Partially res.	...	

NOTES.—Col. (2): Measured angular size in arcsec for the continuum-subtracted emission-line image. Col. (3): Position angle (east of north) for the ELR. Col. (4): Emission-line flux. Col. (5): The log of the equivalent Hα luminosity calculated from col. (4) and conversion factors derived from Koski (1978). Col (6): Cone angle in which the line-emission was contained. Col. (7): Morphological category. Col. (8): Host galaxy PA. Col. (9): Reference for the host galaxy PA.

REFERENCES.—(1) Baum & Heckman 1989a; (2) de Koff et al. 1996; (3) de Vries et al. 1997; (4) Martel et al. 1998.

TABLE 4
RADIO PROPERTIES

Source	Type	Angular Size (arcsec)	PA (deg)	Ref.	log Luminosity (ergs s^{-1} Hz^{-1})
3C 6.1	FR II	25.8	26	13	35.7
3C 17	FR II	30.0	147	5	34.4
3C 31	FR I	1833.0	159	11	32.0
3C 36	FR II	9.0	20	13	35.9
3C 42	FR II	28.0	132	5	34.8
3C 46	FR II	163.0	68	5	34.8
3C 49	CSS	0.98	84	6	35.2
3C 55	FR II	69.0	94	13	35.7
3C 63	FR II	22.0	34	5	34.2
3C 78	FR I	210.0	51	11	32.5
3C 83.1	FR I	680.0	96	11	32.6
3C 84	FR I	492.0	162	11	32.6
3C 93	FR II	34.7	44	17, 20	34.8
3C 93.1	CSS	0.3	165	4, 5	34.2
3C 103	FR II	88	159	5, 8	35.0
3C 109	FR II	96.0	143	5	34.8
3C 111.....	FR II	220.0	62	11	33.5
3C 124	CSS	1.3	7	13	35.8
3C 135	FR II	130.0	70	5	33.9
3C 136.1	FR II	522.0	108	11	33.1
3C 138	CSS	0.6	70	1	35.8
3C 169.1	FR II	38.0	137	8	35.1
3C 171	FR II (dtsb)	30.0	99	2	34.5
3C 172	FR II	103.0	37	13	35.2
3C 175	FR II	48.0	55	10, 20	35.7
3C 184.1	FR II	167.0	157	3	33.7
3C 192	FR II	192.0	124	3	33.2
3C 196.1	CSS	4.0	43	5	34.3
3C 207	FR II	11.4	90	14	35.4
3C 213.1	FR II	43.0	162	5	33.8
3C 219	FR II	184.0	40	5	34.5
3C 220.1	FR II	29.7	79	13	35.4
3C 223	FR II	300.0	164	5	33.8
3C 227	FR II	246.0	86	11	33.7
3C 234	FR II	110.0	64	5	34.5
3C 244.1	FR II	52.0	168	5	35.1
3C 249.1	FR II	12.7	54	20	34.5
3C 263	FR II	43.1	120	19	35.4
3C 264	FR I	91.0	40	11	32.4
3C 268.1	FR II	46.0	83	13	36.0
3C 268.2	FR II	96.0	21	5	34.6
3C 268.3	CSS	1.0	161	5	34.7
3C 268.4	FR II	10.2	42	2, 18	36.1
3C 277.1	CSS	1.5	131	6, 20	34.4
3C 277.3	FR II	29.0	158	11	33.2
3C 280	FR II	12.9	82	1, 10	36.1
3C 284	FR II	176.0	101	5	34.3
3C 297	...[a]	4.0	167	13	36.1
3C 299	FR II	12.0	60	5	34.7
3C 303.1	CSS	1.9	130	6	34.2
3C 305	CSS	14.0	44	10	32.8
3C 305.1	FR II	7.9	11	13	35.5
3C 321	FR II	309.0	131	3	33.5
3C 330	FR II	62.0	62	13	35.5
3C 332	FR II	81.0	20	5	33.8
3C 338	FR I	115.0	85	11	32.9
3C 341	FR II	71.0	50	5	34.9
3C 343.1	CSS	1.0	97	13	35.5
3C 349	FR II	82.0	142	5	34.2
3C 352	FR II	10.2	164	13	35.5
3C 356	FR II	72.0	162	13	35.9
3C 368	FR II	8.5	17	7, 13	36.0
3C 379.1	FR II	76.0	161	5	34.2
3C 380	CSS	1.0	145	2, 9	36.1
3C 381	FR II	69.0	4	5	34.1
3C 382	FR II	179.0	50	11	33.2
3C 390.3	FR II	231.0	145	3	33.5
3C 402	FR I	528.0	163	11	32.1
3C 433	FR II	58.0	172	5	34.2
3C 436	FR II	105.0	172	5, 10	34.4
3C 445	FR II	576.0	171	11	33.3
3C 449	FR I	1742.0	10	11	31.9
3C 452	FR II	277.0	79	11	33.9
3C 454.3	CSS	10.0	128	2, 16	35.7
3C 458	FR II	161	75	12, 15	34.6
3C 465	FR I	375.0	125	11	32.9

NOTES.—Table of radio data from the literature and our maps. The four sources eliminated from our sample due to the lack of a continuum image (see § 3) are not included in this table. Col. (1): 3CR source name. Col. (2): Source classification, given as Fanaroff-Riley type (Fanaroff & Riley 1974), compact steep-spectrum (CSS) source (from de Vries et al. 1997), or other morphology. Col. (3): Angular size in arcseconds. Col. (4): Position angle of the radio source, generally measured from hotspot to hotspot. Col. (5): Reference for the angular size. Col. (6): Logarithm of the radio luminosity, calculated at 178 MHz.

[a] We were unable to find good maps or a FR classification for this source.

REFERENCES.—(1) Akujor & Garrington 1995; (2) Allington-Smith 1984; (3) Baum & Heckman 1989a; (4) Dallacasa et al. 1995; (5) de Koff et al. 1996; (6) de Vries et al. 1997; (7) Dunlop & Peacock 1993; (8) Leahy et al. 1986; (9) Lister & Homan 2005; (10) Mackay 1969; (11) Martel et al. 1999; (12) McCarthy et al. 1995; (13) McCarthy et al. 1997; (14) Mullin et al. 2006; (15) Nilsson et al. 1993; (16) Perley 1982; (17) Price et al. 1993; (18) Reid et al. 1995; (19) Swarup et al. 1984; (20) this paper.

which both [O II] and [O III] are obtained show that the estimated large-scale PAs are consistent (e.g., Tilak et al. 2005).

Another possible bias is the extent of the ELRs for different emission lines. Studies of single objects in multiple emission lines indicate typical ratios in the extended emission of ~1–6 for [O III]/[O II] and ~1–4 for [O III]/Hα (e.g., Tilak et al. 2005; Solórzano-Iñarrea & Tadhunter 2003; Robinson et al. 2000). Thus, as the transition between lines is made, the ELR should be smaller for [O II] than for [O III]. As is discussed in § 5.3, the opposite is found.

Over the redshift range of our sample ($0.017 \leq z \leq 1.406$), the expected $(1 + z)^4$ dimming of surface brightness is a factor of ~30; although the details will depend on the actual surface brightness profiles. Thus, both the transition from [O III] to [O II] and the $(1 + z)^4$ effect should result in apparently smaller ELR at higher redshift. Despite this, we see emission-line size increasing with redshift (see § 5.3), suggesting that this result is real.

In order to investigate the possible effect of an instrumental sensitivity selection effect on the detection of alignment, we redshifted the faintest level in the emission-line images to see what would be detected if located at $z = 0.5$ (just prior to the onset of strong alignment). None of the misaligned sources showed any alignment when viewed using these modified levels. This indicates that the alignment effect is not due to a selection effect of the sensitivity of the instrument, but rather to some other inherent attribute of the source and its environment.

5.1.1. *Comparison with Ground-based Data*

The emission-line images from *HST* were compared with previous studies using ground-based imaging (Fig. 3). Morphologies and PAs were generally consistent between the two sets consistent with the hypothesis that the nebulae PAs do not exhibit

TABLE 5
STATISTICAL CORRELATIONS

Relationship	Kendall's τ	P_τ	Spearman's ρ	P_ρ
Emission-line luminosity vs. ΔPA	−0.6577	0.040	−0.474	0.0044
Emission-line luminosity vs. ΔPA ($z < 0.6$)	−0.5417	0.0258	−0.404	0.0222
Emission-line luminosity vs ΔPA ($0.1 < z < 0.6$)	−0.6338	0.0219	...	...
Emission-line luminosity vs. host mag	−0.8734	0.0003	−0.611	0.0005
Emission-line luminosity vs. radio luminosity	1.095	0.0000	0.740	0.0000
Emission-line nebulae size vs. radio luminosity	0.7177	0.0039	0.487	0.0067
Emission-line nebulae size vs. radio luminosity ($z < 0.6$)	0.6483	0.0119	0.442	0.0172
Emission-line nebulae size vs. z	0.6976	0.0050	0.499	0.0055
Emission-line nebulae size vs. z ($z < 0.6$)	0.6253	0.0152	0.458	0.0136
ΔPA vs. radio size	0.6050	0.0105	0.455	0.0080
ΔPA vs. size ratio	1.0099	0.0001	0.684	0.0003

NOTE.—The probabilities given are the probabilities that a correlation is not present.

large changes in PA as a function of size scale. However, because of the lower surface brightness sensitivity of the *HST* WFPC2 camera, the *HST* images show only the brighter inner regions of the nebulae. Thus, the *HST* measured sizes and emission-line fluxes tend to be smaller than those measured on ground based images.

Figure 4 shows a comparison of the distribution of PA differences from ground-based data (Baum et al. 1988; Rigler et al. 1992; McCarthy et al. 1995) with our *HST* data. There is a suggestion that the *HST* data shows an alignment effect which is weaker than seen in the ground-based data at the same redshifts. The Kolmogorov-Smirnov (KS) test indicates that the distribution of PA differences in the *HST* data is consistent with a uniform distribution of angles, while the ground based data are not (see Table 7). If larger samples confirm this result, this may be due to the *HST* data mainly being sensitive to the higher surface brightness, more compact emission, suggesting that the alignment effect is mainly produced in fainter, more extended emission-line gas.

5.2. *Relative Sizes of the Emission-Line Region and the Radio Source*

We computed the "size ratio" comparing the relative projected linear sizes of the radio source and the high surface brightness emission-line region. The linear sizes for FR II and CSS sources were measured from hotspot to hotspot, and the linear sizes for FR I sources were measured across the overall extent. Linear sizes for the emission-line regions were measured roughly along the long axis (if such an axis existed). Comparing the relative sizes of the radio source and ELR with the relative alignment indicates that sources with similar radio and ELR sizes are more frequently aligned than sources in which the ELR is much smaller than the radio source (Fig. 5). This is true at all redshifts (Fig. 5). We also note that all six of the small sources ($D < 15$ kpc, i.e., CSS) are well aligned (Fig. 6). All six of these have size ratios between $\sim$0.3 and $\sim$6. These results suggest that the alignment at low-redshift results when the source is smaller/younger and of a similar size as the nebula. This is consistent with suggestions that the alignment is due to mechanical energy input from the radio source (e.g., de Vries et al. 1999; Axon et al. 2000; Best et al. 2000; Inskip et al. 2002a, 2002b). At low redshifts, suitable gas clouds are likely to exist only on the scale of the host galaxy.

In addition, 13 of the 29 large sources (size greater than 50 kpc) also show alignment to within 30°. These sources are much bigger than their emission-line nebulae (factors of 10–100). Some of this alignment may be produced by chance if the PAs differences in at least some low-z sources are randomly distributed. However, some of the alignment may be real, since we suspect the effect is starting to turn on at these redshifts. Diagnostic line ratios and kinematics indicate that shocks are important when the radio source size is comparable to the aligned emission-line nebula size and that photoionization dominates when the radio source is much larger than the nebula (e.g., Best et al. 2000; Inskip et al. 2002a; Moy & Rocca-Volmerange 2002; O'Dea et al.2002; Labiano et al. 2005). Thus, in these large sources, the alignment may be produced by photoionization from the central AGN along the "ionization cone." Recombination times for warm gas ($T \sim 10^4$ K) are roughly 10^3 yr (Osterbrock 1989) while the lifetimes of the radio sources are roughly 10^7–10^8 yr, indicating the ionizing mechanism must be on-going throughout the lifetime of the source.

5.3. *Emission-Line Nebula Size and Luminosity*

The size of the high surface brightness ELR increases with increasing radio power (Fig. 7) and/or with increasing redshift (Fig. 8). Both correlations are somewhat weaker for just the $z <$ 0.6 objects. At higher redshifts, dense gas clouds are found on

TABLE 6
STATISTICAL NONCORRELATIONS

Relationship	Kendall's τ	P_τ	Spearman's ρ	P_ρ
ΔPA vs. z	−0.3874	0.0913	−0.238	0.1540
ΔPA vs. emission-line nebulae asymmetry	−0.3126	0.2243	−0.222	0.2327
Emission-line nebulae luminosity vs. radio size	−0.3624	0.0423	−0.280	0.0330
Emission-line nebulae size vs. radio size	−0.3484	0.1686	−0.283	0.1216

NOTE.—The probabilities given are the probabilities that a correlation is not present.

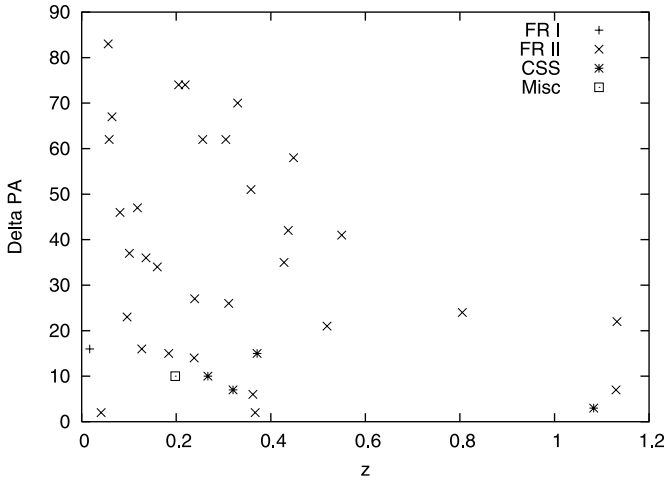

FIG. 2.—Relative alignment of the radio source and ELR as a function of redshift. No correlation was present with the Kendall's τ test giving a noncorrelation probability of 0.0913 and Spearman's ρ test giving a probability of 0.1540 of a correlation not being present.

increasingly larger scales culminating in the large Lyα halos surrounding powerful radio galaxies (van Ojik et al.1997; Reuland et al. 2003). Of course, the radio luminosity will also increase with redshift in flux density limited samples, meaning the correlations may be related. Studies which attempt to break the redshift-radio power degeneracy suggest that the alignment depends on both redshift and radio power (e.g., Inskip et al. 2002b, 2005). The more powerful radio sources can provide both more mechanical energy and more ionizing photons (Baum & Heckman 1989a; Rawlings & Saunders 1991). Thus, both the presence of gas on larger scales as well as the larger energy input from the radio source could result in the emission-line size increasing with redshift and radio power.

Comparing the luminosity of the ELR with the relative alignment (Fig. 9) indicates aligned sources have more luminous ELRs. The correlation becomes weaker for the redshift range $z < 0.6$. We find that the correlation is further weakened if we also exclude $z < 0.1$ (Fig. 9). The existence of the (weak) correlation at $z < 0.6$ suggests that the radio source provides additional energy to the emission-line gas along the direction of the radio axis and thus, there is a "real," although weak, alignment effect at these low redshifts.

6. CONCLUSIONS

We present WFPC2 LRF images of selected emission lines in a sample of 3CR radio galaxies with bright emission lines. We detect clumpy, high surface brightness emission-line gas with a wide range of morphologies. We examine the properties of the emission-line gas and its relationship to the radio source, and in particular the nature of the alignment effect at $z < 0.6$, where the effect is beginning to become important.

We find there is a weak alignment effect in our low-z sample ($z < 0.6$). The effect is clearly weaker than seen at high redshifts and is also somewhat weaker than seen at similar redshifts in ground-based data. This suggests that the alignment effect is dominated by the more extended lower surface brightness emission-line gas which falls below our detection threshold in WFPC2.

The alignment at low redshift is strong when the radio source and the nebula are both of the order of galactic scales (e.g., CSS sources). This implies there is mechanical energy input from the radio source as it propagates through the ambient gas in the host galaxy (e.g., de Vries et al. 1999; Axon et al. 2000).

There is a weak trend for the nebulae in the aligned sources (at all radio/optical size ratios) to have higher line luminosity. This suggests that the radio source preferentially provides energy to gas which is along the radio source axis. This is likely to be predominantly mechanical energy when the radio source and

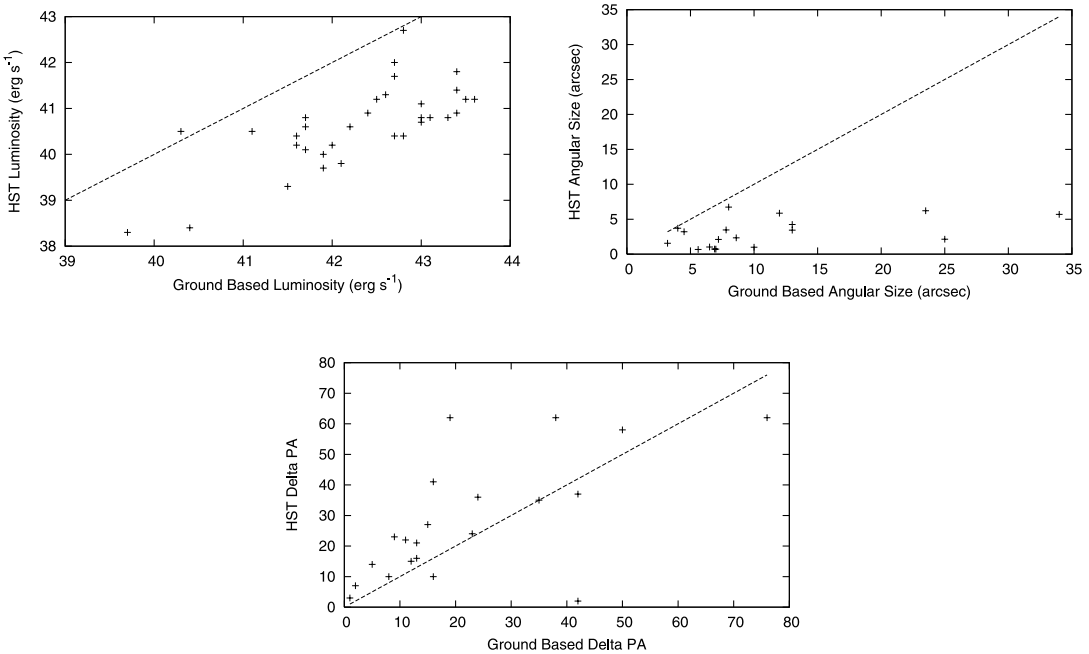

FIG. 3.—*Top Left*: Comparison of the *HST* luminosities from our data with ground based data from previous studies (Baum & Heckman 1989a; McCarthy et al. 1995). The *HST* luminosities are much lower due to the lower surface brightness sensitivity of WFPC2. *Top Right*: Comparison of the angular sizes in our *HST* data with ground based data. The extended emission is of low surface brightness, and we do not detect the full extent of the ELR as seen from the ground. *Bottom*: Comparison of the ΔPA derived from the *HST* data and ground based data. While many of the values are quite similar, some are significantly different. The line in all plots is $y = x$.

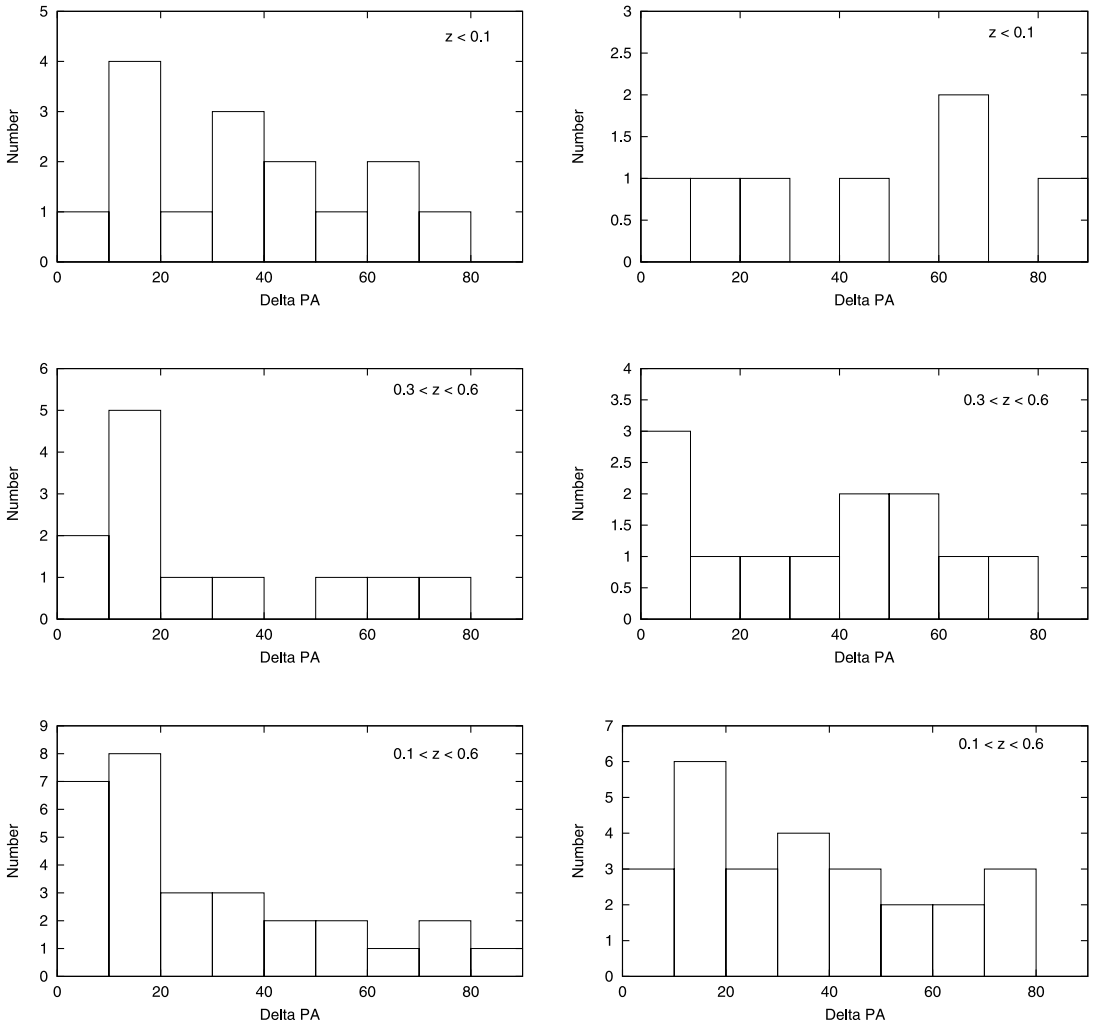

FIG. 4.—Histograms of relative alignment between the emission-line region and the radio source for various redshift ranges. The left column plots ground-based data compiled in McCarthy et al. (1995), while the right column shows our *HST* WFPC2 data. The top two plots are for $z < 0.1$. The middle row is for $0.3 < z < 0.6$ and the bottom row is for $0.1 < z < 0.6$.

TABLE 7

RELATIVE ALIGNMENT STATISTICAL RESULTS

ΔPA Category	Data Points	Max ABS Discrepancy	Significance (%)
This paper (*HST*), $z < 0.1$	7	0.169	98.8
This paper (*HST*), $0.3 < z < 0.6$	13	0.157	90.5
This paper (*HST*), $0.1 < z < 0.6$	26	0.152	58.8
McCarthy et al. (1995), $z < 0.1$	15	0.171	77.0
McCarthy et al. (1995), $0.3 < z < 0.6$	12	0.44	1.90
McCarthy et al. (1995), $0.1 < z < 0.6$	30	0.343	0.168

NOTES.—KS test results comparing the distribution of ΔPA (see Fig. 4) with that of a uniform distribution. Col. (3) indicates the likelihood that the two distributions are the same. Note that the KS test works best for at least 40 points. Our study has fewer points and the KS test results may be unreliable for some categories.

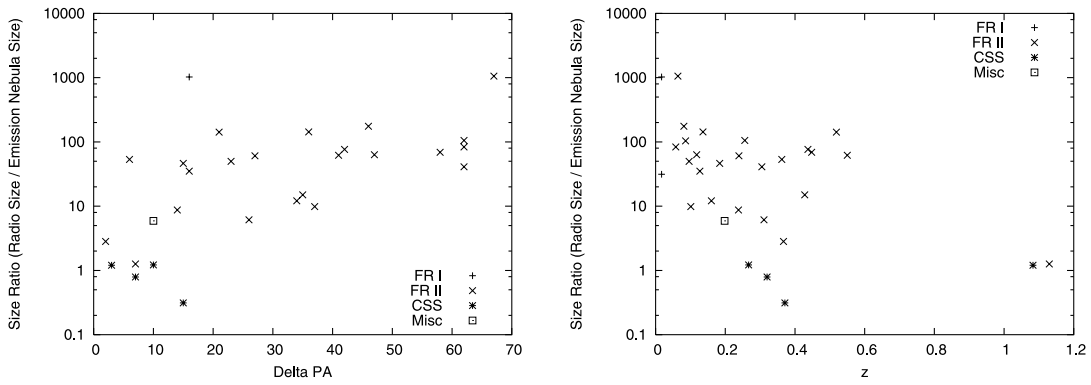

FIG. 5.—*Left*: Calculated size ratio between the radio source and the emission-line region as a function of alignment between the two. The sources with size ratios of roughly one have optical morphologies which are closely aligned with the radio source. Both Kendall's τ and Spearman's ρ tests indicate the presence of a correlation with noncorrelation probabilities of 0.0001 and 0.0003, respectively. *Right*: Size ratio as a function of z. The sources with size ratios near unity are found at both high and low redshifts.

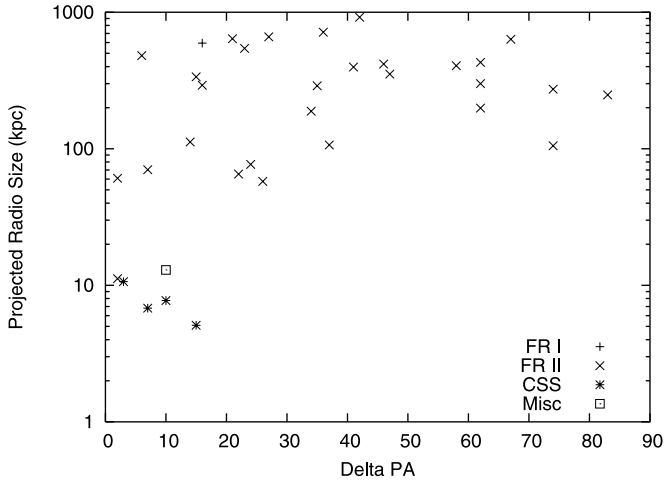

FIG. 6.—Projected radio size as a function of the relative alignment between the radio source and the emission-line nebulae. All of the small sources are aligned while only some of the large sources are aligned.

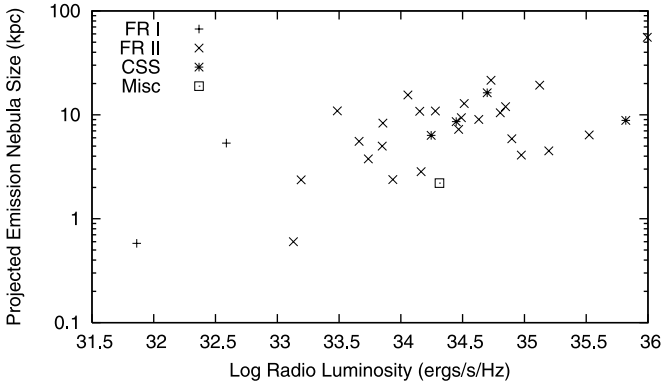

FIG. 7.—Projected emission-line nebulae size against logarithm of the radio luminosity. The probabilities of this being a noncorrelation are 0.0039 (Kendall's τ) and 0.0067 (Spearman's ρ) for the whole sample and are 0.0119 (Kendall's τ) and 0.0172 (Spearman's ρ) for $z < 0.6$.

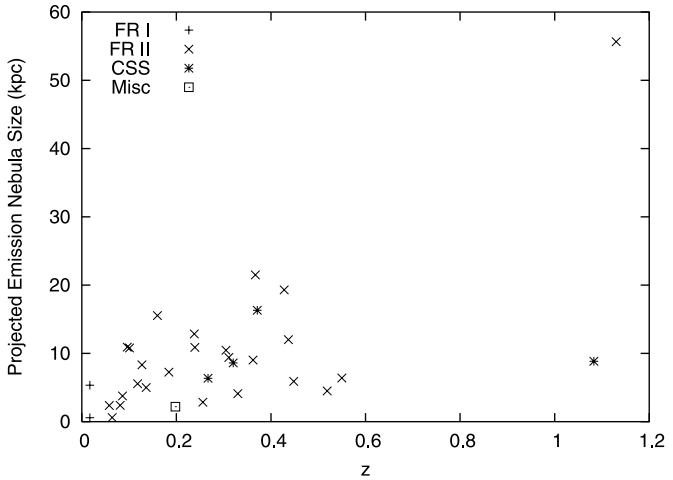

FIG. 8.—Projected emission-line nebulae size as a function of redshift. The probabilities of this being a noncorrelation are 0.0050 (Kendall's τ) and 0.0055 (Spearman's ρ) for the whole sample and are 0.0152 (Kendall's τ) and 0.0136 (Spearman's ρ) for $z < 0.6$.

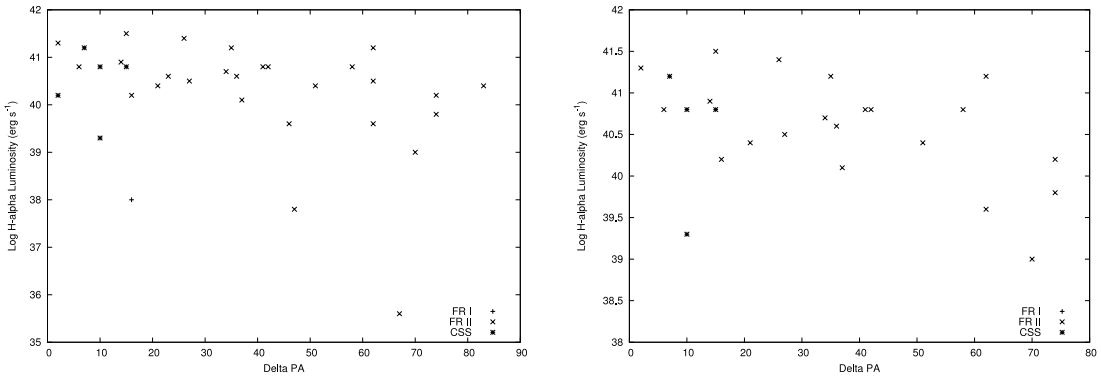

FIG. 9.—*Left*: Logarithm of the emission-line nebulae luminosity against the relative alignment between the radio source and the emission-line nebulae. The probabilities of this being a noncorrelation are 0.0083 (Kendall's τ) and 0.0134 (Spearman's ρ) for the whole sample and are 0.0356 (Kendall's τ) and 0.0473 (Spearman's ρ) for $z < 0.6$. *Right*: Same as left plot, but for sources with $0.1 < z < 0.6$ only. The probability of this being a noncorrelation is 0.0429 (Kendall's τ).

nebulae have similar sizes and predominantly photoionization when the radio source is much larger than the nebula (e.g., Best et al. 2000; Inskip et al. 2002a; Moy & Rocca-Volmerange 2002; O'Dea et al.2002; Labiano et al. 2005).

There is a weak trend for the size of the high surface brightness emission-line nebulae to increase with increasing radio power and/or redshift over the range $z < 0.6$. This may be due to both the increasing presence of gas on large scales and the ability of the more powerful radio sources to provide additional mechanical energy and/or ionizing photons as a function of redshift.

Thus, there is evidence for a modest excess of aligned sources at low redshift ($z < 0.6$). The alignment is strong when the radio source and emission-line nebula are both on galactic scales. There are also weak trends for the aligned emission-line nebulae to be more luminous, and for the emission-line size to increase with redshift and radio power. The combination of these results suggests that there is a limited but real capacity for the radio source to influence the properties of the emission-line nebulae at these low redshifts.

Support for program 5957 was provided by NASA through a grant from the Space Telescope Science Institute, which is operated by the Association of Universities for Research in Astronomy, Inc., under NASA contract NAS 05-26555. This research has made use of the NASA/IPAC Extragalactic Database (NED), which is operated by the Jet Propulsion Laboratory, California Institute of Technology, under contract with the National Aeronautics and Space Administration. This research has also made use of NASA's Astrophysics Data System Bibliographic Services. We are grateful to the referee for comments which helped to clarify the presentation of the results.

Facilities: HST (WFPC2), VLA (NRAO)

APPENDIX

INDIVIDUAL SOURCE NOTES

3C 46 (Figs. 10 and 11) is a large FR II radio source. The emission-line nebula and the radio source are not well aligned. The optical continuum image seems to show a double structure. However, the line emission is predominantly in the southern portion.

3C 49 (Figs. 12 and 13) was a marginal detection. A smoothed image was used for the overlay and the lowest contour is 2 σ.

3C 84 (Figs. 14 and 15) has a diffraction cross in the emission-line image. A sufficiently deep 5 or 8 GHz radio map was not available and could not be found in archival data, so an overlay is not shown. The line emission is symmetrically distributed within the host galaxy so there is no meaningful position angle.

3C 98 (Fig. 16) did not have a continuum image so only the narrowband image is presented here.

3C 109 (Figs. 17 and 18) has an emission-line region which is not aligned with the radio source. The ELR is in a disk which is perpendicular to the radio jet.

3C 124 (Figs. 19 and 20) has an emission-line region which is very closely aligned with the radio source. The exact center of the host galaxy is not well determined for our images.

3C 135 (Figs. 21 and 22) features an emission-line region which is closely aligned with the overall radio source. The radio source is very large compared to the emission-line region. The emission-line region is elongated along the radio jet axis and features a disconnected region of emission toward the Northwest hotspot.

3C 171 (Figs. 23 and 24) has an emission-line region tracing the jets, linking the core to the hotspots. There is emission around the east hotspot. The ELR structure has been discussed in detail in Tilak et al. (2005).

3C 223 (Figs. 25 and 26) does not have an aligned emission-line nebula. However, the core shows slight extension in the direction of the emission-line nebulae.

3C 234 (Figs. 27 and 28) is aligned with the radio source, and the core shows slight extension along the major axis of the nebula. There are also filaments extending almost perpendicular to the radio axis. The broad lines in 3C 234 are highly polarized, so it is not surprising the properties of this source are similar to that of NLRGs (Antonucci 1984).

3C 249.1 (Figs. 29 and 30) has an ELR which does not have a preferential alignment with the radio source. It features two regions of emission which are disconnected from the nuclear emission at the radio core.

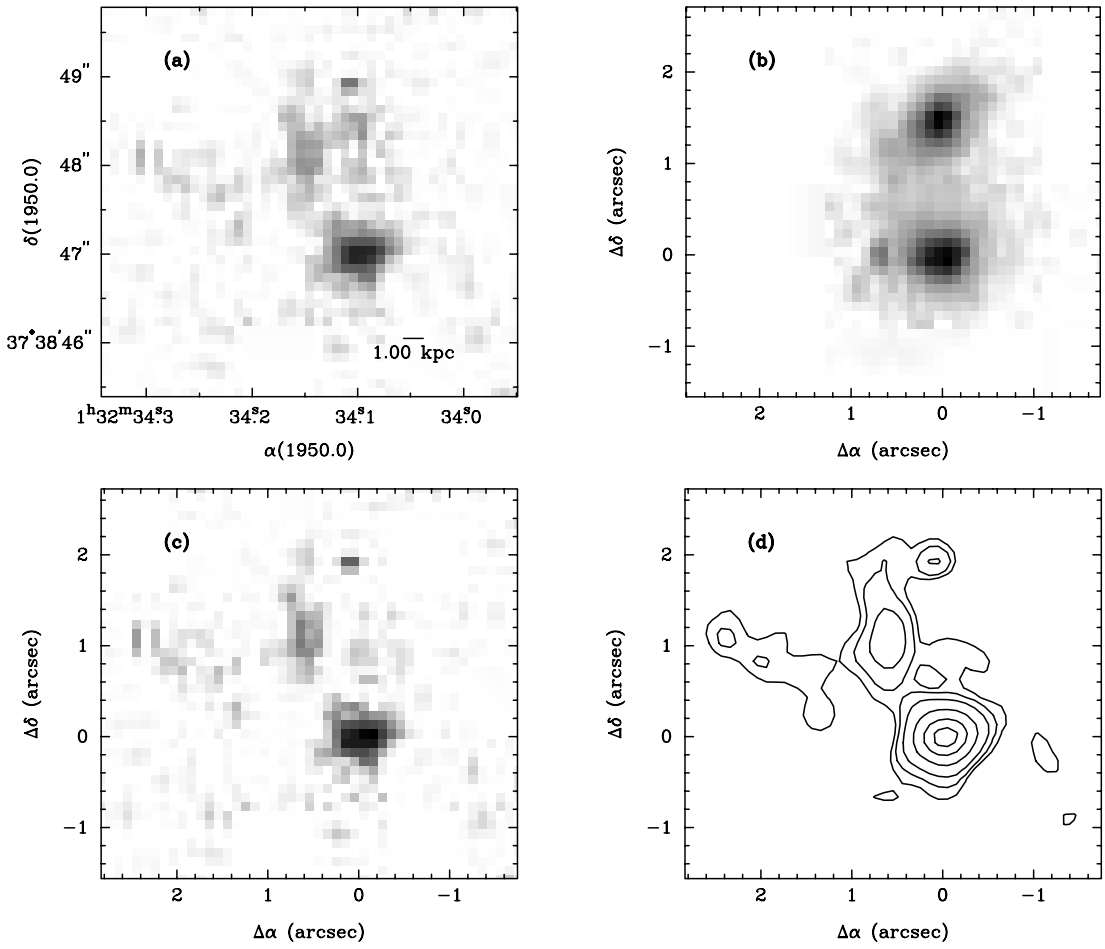

FIG. 10.—3C 46 (optical montage). Starting at the top left, going clockwise: LRF image, broadband image, continuum-subtracted image (*contours*), and continuum-subtracted image (*gray scale*).

3C 268.2 (Figs. 31 and 32) shows an emission-line nebula which is closely aligned with the radio source. The ELR is asymmetrical around the center of the host galaxy (measured from the broadband continuum image). There is little to no line emission detected from the nucleus in our images. The core was not detected in the radio maps; however, the location was inferred using the WCS coordinates given on NED. As the core was not detected in the radio map, we are unable to examine spatial coincidence of the ELR and the radio core, but are still able to measure the alignment of the ELR and radio source.

3C 268.3 (Figs. 33 and 34) is an aligned CSS source (de Vries et al. 1999). The emission extends beyond the radio source. Registration of the radio core and the emission-line image was problematic due to the lower resolution of the optical image. 3C 268.3 shows broad lines, indicating this source may not be in the plane of the sky.

3C 273 (Fig. 35) did not have a continuum image; however, the narrowband image is presented here.

3C 284 (Figs. 36 and 37) has and ELR which is composed of three separate components in our images. The PA along the overall structure is not aligned with the source. However, taking an "inner PA" of the central structure gives the alignment with the radio source, so we consider this ELR aligned with the radio source.

3C 299 (Figs. 38 and 39) has aligned emission-line and radio morphology. Both the emission-line region and the radio source are asymmetric about the center of the host galaxy.

3C 303.1 (Figs. 40 and 41) has an emission-line nebula which is of similar size in our WFPC images as the radio source. They are closely aligned. The emission-line region is symmetrical about the nucleus and is elongated along the radio axis.

3C 305 (Figs. 42 and 43) has an emission-line region that is aligned with the jets and hotspots. However, the emission extends beyond the extent of the radio source, limiting the probability of shock ionization as a primary mechanism for transferring energy to ambient gas (Jackson et al. 1995).

3C 321 (Figs. 44 and 45) has the ELR aligned with the radio source. Because of the dust lane (noted in Martel et al. 1998) determining the proper center of the host galaxy is problematic.

3C 323.1 (Fig. 46) did not have a continuum image for subtraction, but the LRF image is presented here.

3C 341 (Figs. 47 and 48) does not show alignment between the emission-line nebula and the radio source. The size of the ELR is comparable to a resolution element in the radio map, making examination of spatial coincidence problematic.

3C 368 (Figs. 49 and 50) shows close alignment between the ELR and the radio source.

3C 379.1 (Figs. 51 and 52) shows an ELR which is not aligned with the radio source. The ELR is smaller than the resolution of our radio image.

3C 381 (Figs. 53 and 54) does not show alignment between the emission-line nebula and the radio source.

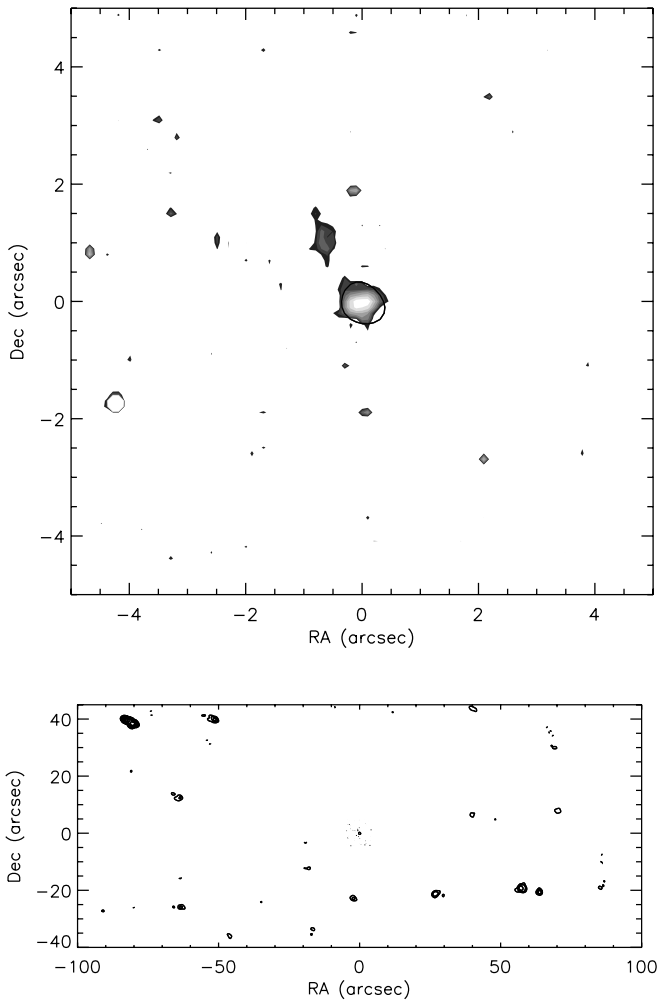

FIG. 11.—3C 46 (radio/optical overlay). Radio is shown in contours. Optical is shown in gray scale. *Left*: Close-up of the core. *Right*: View of the overall radio source. Radio levels are (1.215, 1.719, 2.431, 3.437, 4.861, 6.875, 9.722, 13.750, 19.445, 27.499) mJy. Optical levels are (0.094, 0.133, 0.188, 0.266, 0.377, 0.533, 0.754, 1.066) $\times 10^{-14}$ ergs s^{-1} arcsec^{-2}. Both images have the same levels. Radio map from Neff et al. (1995).

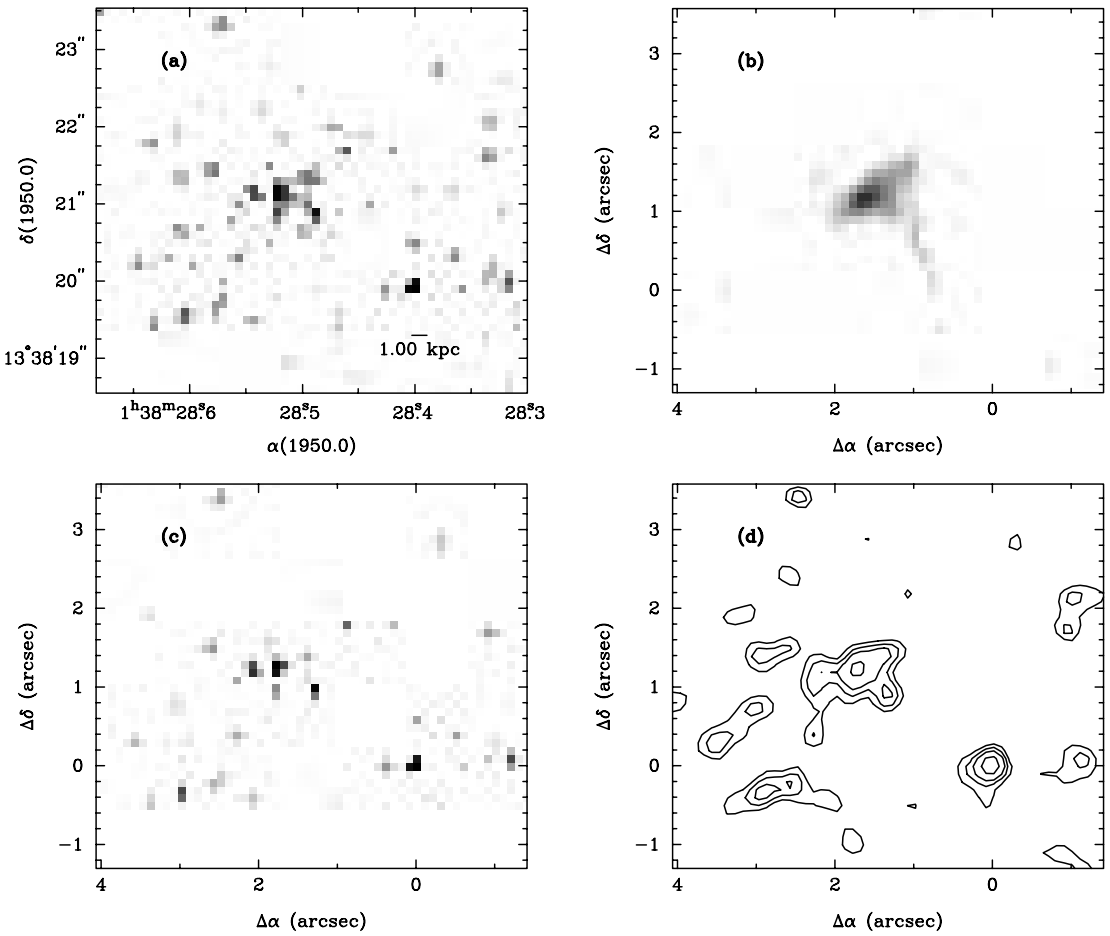

FIG. 12.—3C 49 (optical montage). Starting at the top left, going clockwise: LRF image, broadband image, continuum-subtracted image (*contours*), and continuum-subtracted image (*gray scale*).

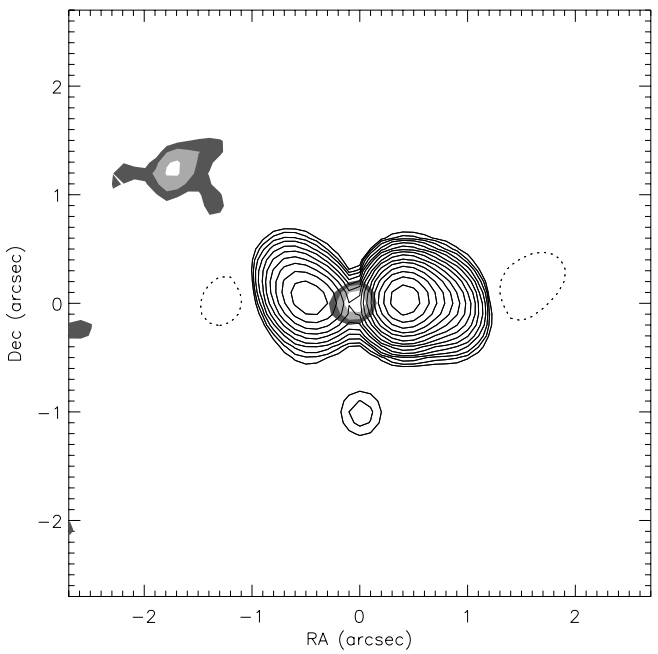

FIG. 13.—3C 49 (radio/optical overlay). Radio is shown in contours. Optical is shown in gray scale. Radio levels are (3.555, 5.028, 7.110, 10.055, 14.220, 20.110, 28.440, 40.220, 56.880, 80.440, 113.760, 160.881, 227.520, 321.762, 455.040) mJy. Optical levels are (0.030, 0.043, 0.055) $\times 10^{-14}$ ergs s^{-1} arcsec^{-2} The radio map is from Neff et al. (1995).

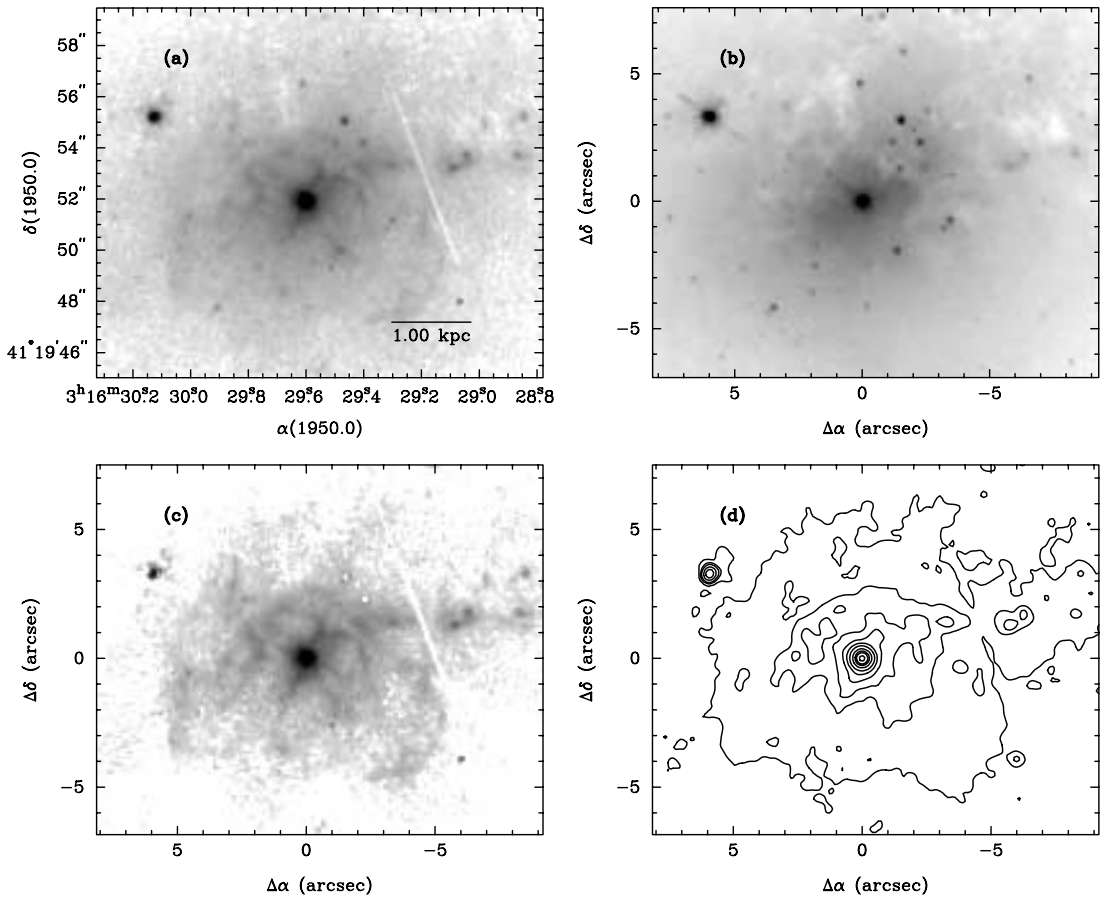

FIG. 14.—3C 84 (optical montage). Starting at the top left, going clockwise: LRF image, broadband image, continuum-subtracted image (*contours*), and continuum-subtracted image (*gray scale*).

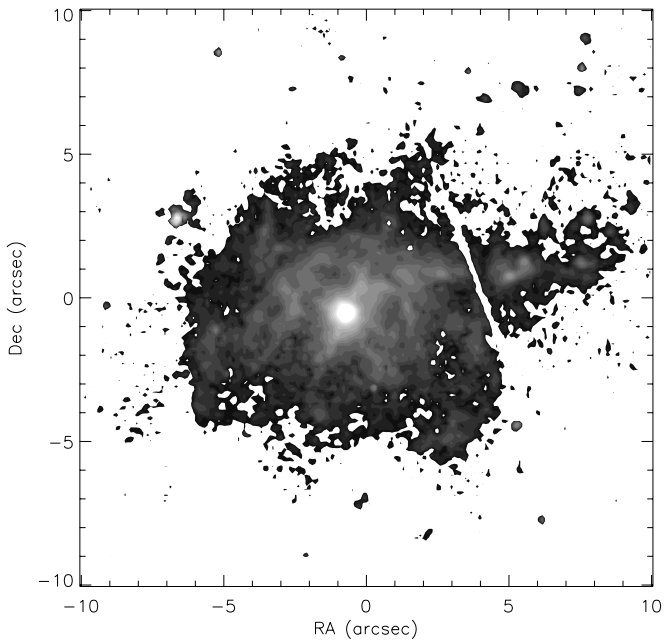

FIG. 15.—3C 84 (emission line only). Optical is shown in gray scale. Optical levels are (0.081, 0.114, 0.161, 0.228, 0.323, 0.457, 0.647, 0.915, 1.295, 1.831, 2.589, 3.662, 5.180, 7.325, 10.359, 14.650) $\times 10^{-14}$ ergs s^{-1} arcsec^{-2}. (Note that in radio maps 3C 84 is highly core dominated. A worthwhile 5 or 8 GHz radio map could not be located, so only the emission-line image is presented.)

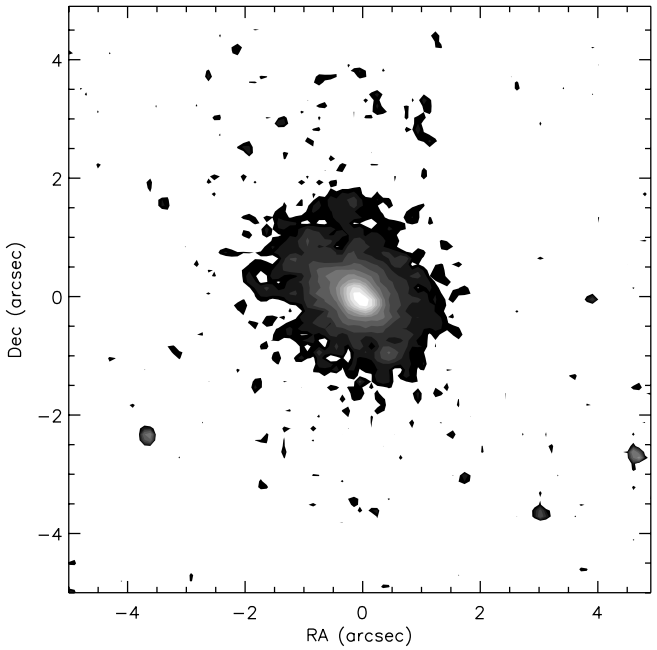

FIG. 16.—3C 98 (narrowband image). This is the narrowband optical (LRF) image. The levels are (0.074, 0.104, 0.148, 0.209, 0.296, 0.419, 0.593, 0.838, 1.186, 1.677, 2.372, 3.354) $\times 10^{-14}$ ergs s^{-1} arcsec^{-2}.

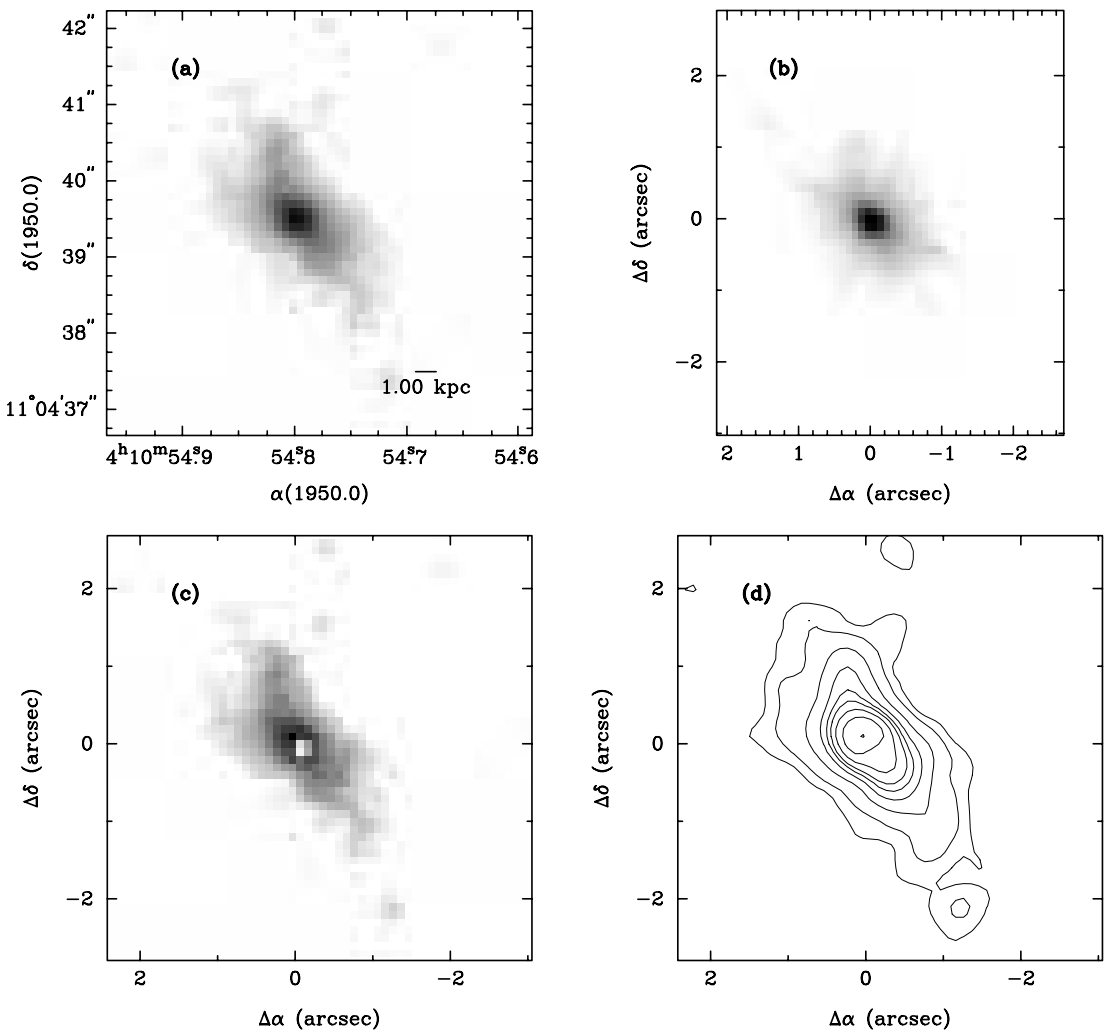

FIG. 17.—3C 109 (optical montage). Starting at the top left, going clockwise: LRF image, broadband image, continuum-subtracted image (*contours*), and continuum-subtracted image (*gray scale*).

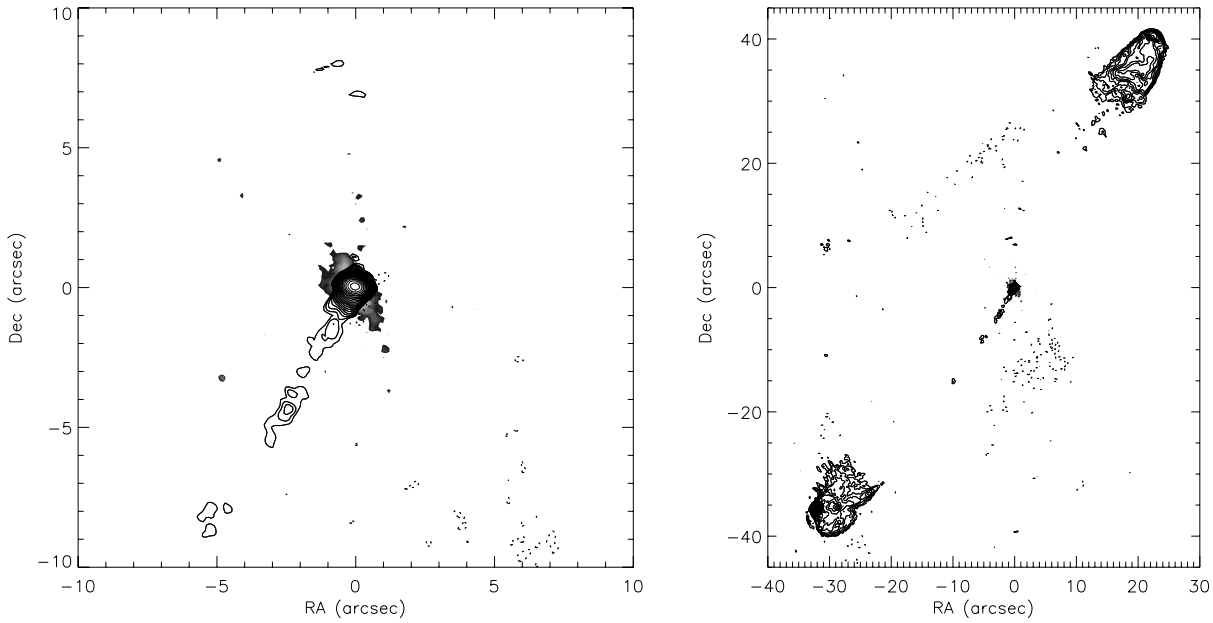

FIG. 18.—3C 109 (radio/optical overlay). Radio is shown in contours. Optical is shown in gray scale. *Left*: Close-up of the core. *Right*: View of the overall radio source. Radio levels are (0.199, 0.281, 0.398, 0.563, 0.796, 1.125, 1.591, 2.250, 3.182, 4.501, 6.365, 9.001, 12.730, 18.002, 25.459, 36.005, 50.918, 72.009, 101.837, 144.019) mJy. Optical levels are $(0.077, 0.110, 0.155, 0.220, 0.311, 0.440, 0.622, 0.880, 1.249) \times 10^{-14}$ ergs s^{-1} arcsec^{-2}. Both images have the same levels.

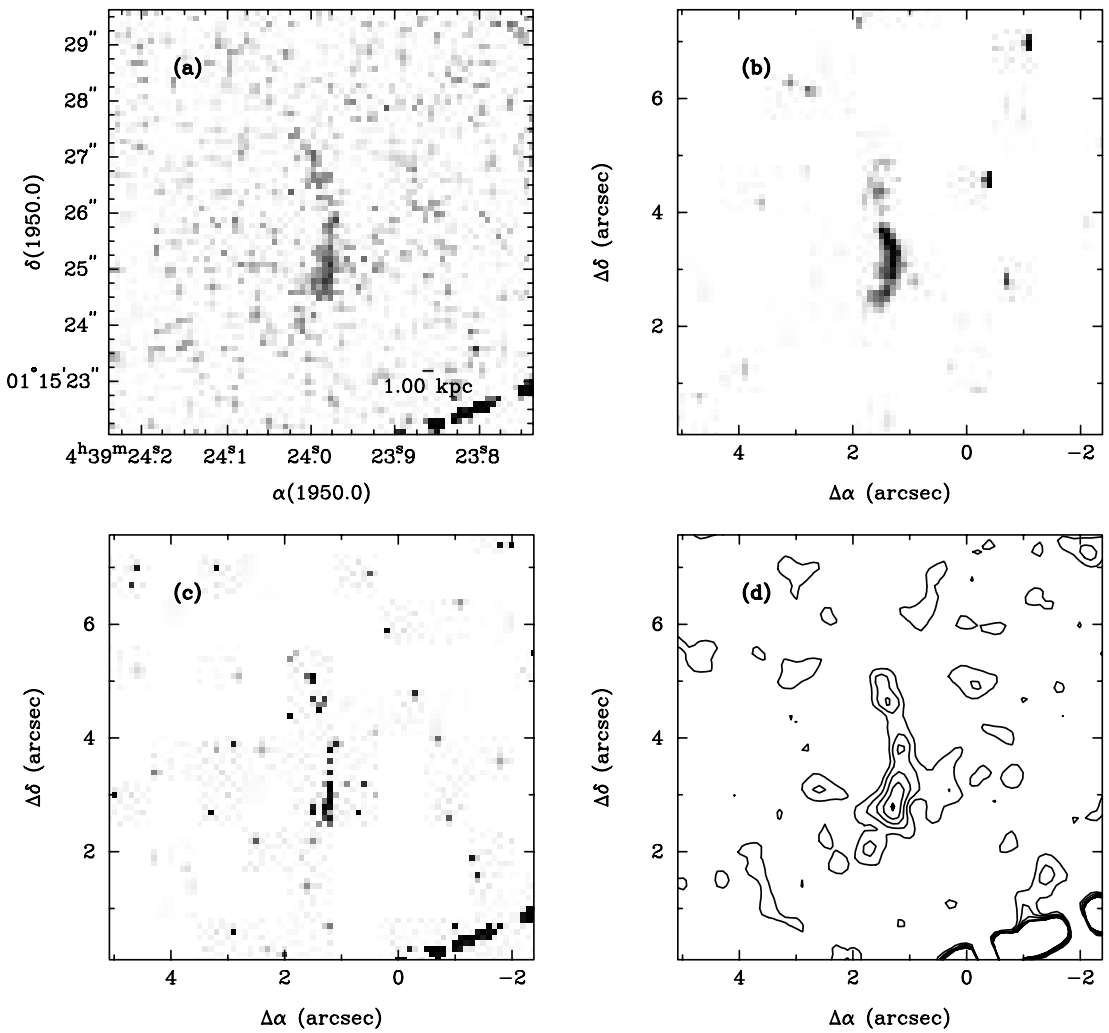

FIG. 19.—3C 124 (optical montage). Starting at the top left, going clockwise: LRF image, broadband image, continuum-subtracted image (*contours*), and continuum-subtracted image (*gray scale*).

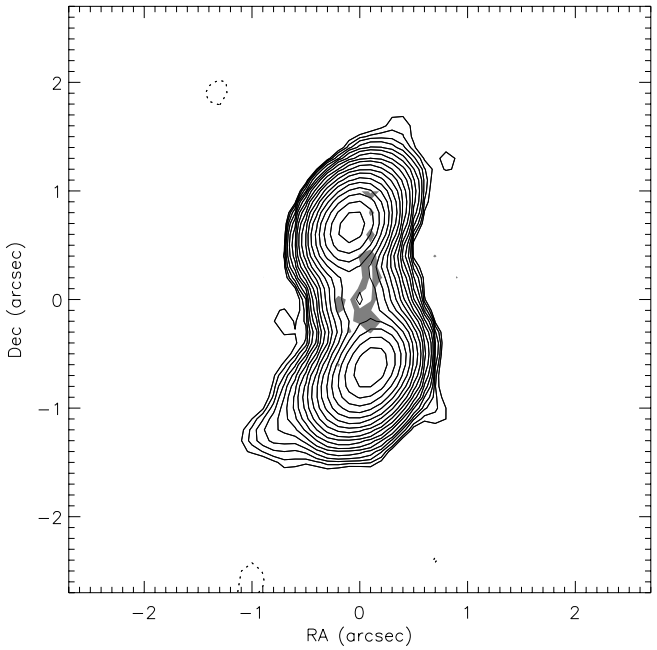

FIG. 20.—3C 124 (radio/optical overlay). Radio is shown in contours. Optical is shown in gray scale. Radio levels are (0.182, 0.258, 0.365, 0.516, 0.730, 1.032, 1.459, 2.064, 2.918, 4.127, 5.837) mJy. Optical levels are (0.107, 0.152) $\times 10^{-14}$ ergs s^{-1} arcsec^{-2}.

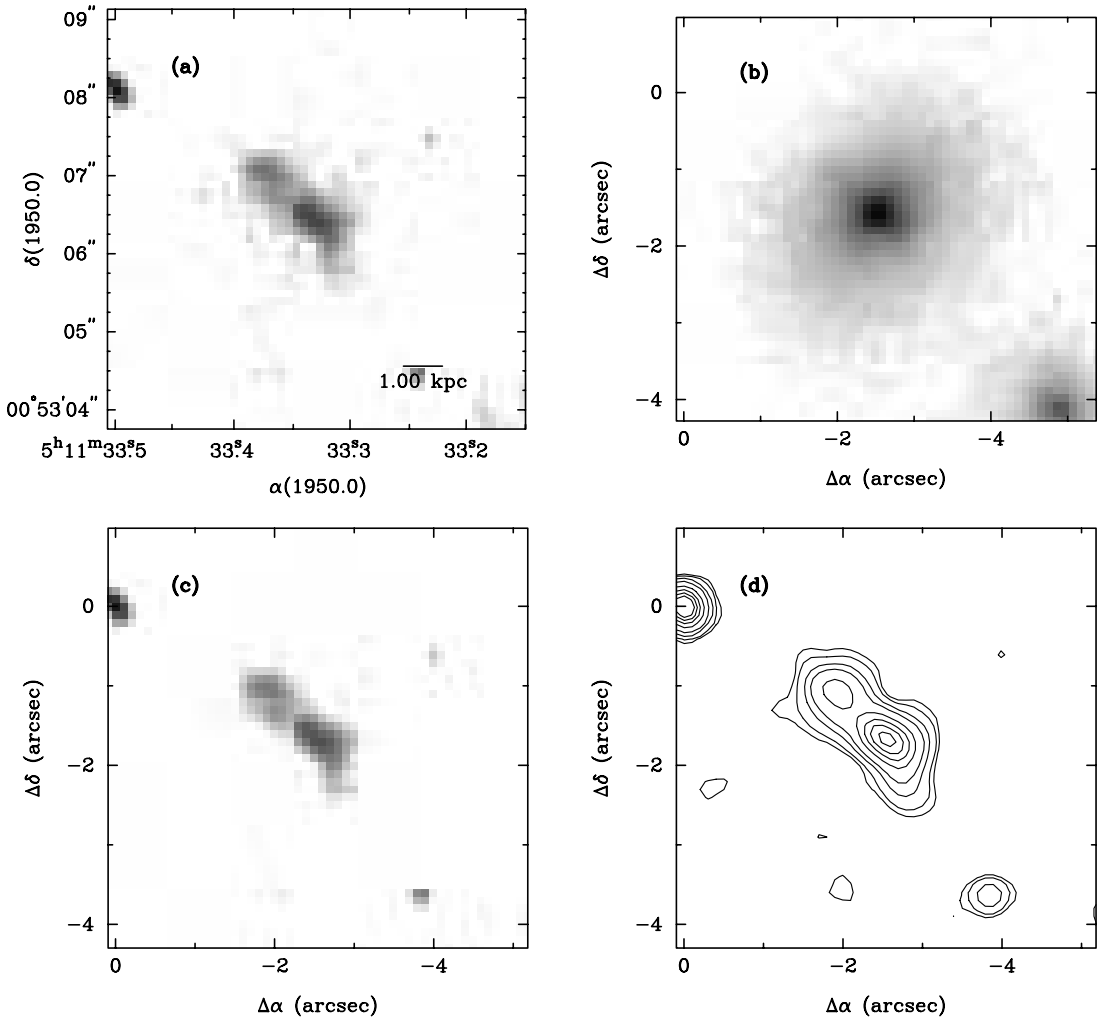

FIG. 21.—3C 135 (optical montage). Starting at the top left, going clockwise: LRF image, broadband image, continuum-subtracted image (*contours*), and continuum-subtracted image (*gray scale*).

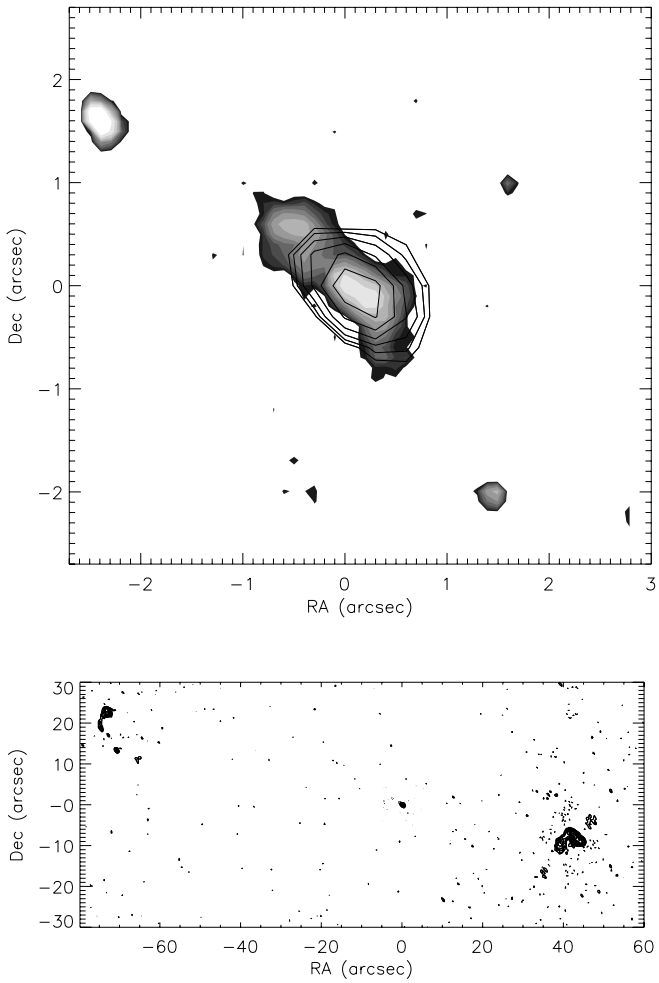

FIG. 22.—3C 135 (radio/optical overlay). Radio is shown in contours. Optical is shown in gray scale. *Top*: Close-up of the core. *Bottom*: View of the overall radio source. Radio levels are (0.151, 0.214, 0.303, 0.429, 0.606, 0.857, 1.212, 1.714, 2.424, 3.428, 4.848, 6.856) mJy. Optical levels are (0.160, 0.226, 0.320, 0.453, 0.640, 0.905, 1.281, 1.811, 2.562, 3.623) $\times 10^{-14}$ ergs s^{-1} arcsec^{-2}. Both images have the same levels.

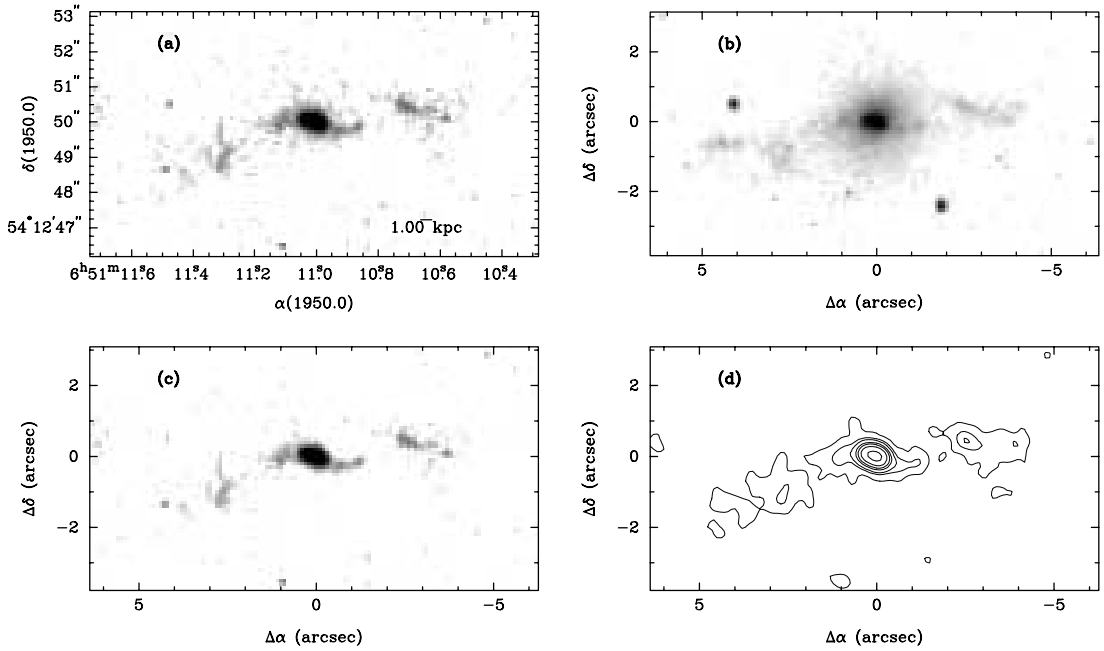

FIG. 23.—3C 171 (optical montage). Starting at the top left, going clockwise: LRF image, broadband image, continuum-subtracted image (*contours*), and continuum-subtracted image (*gray scale*).

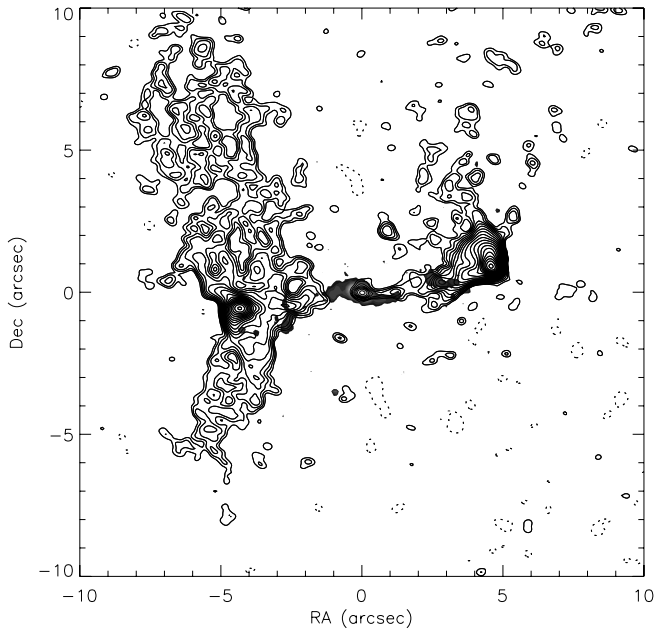

FIG. 24.—3C 171 (radio/optical overlay). Radio is shown in contours. Optical is shown in gray scale. Radio levels are (0.164, 0.231, 0.327, 0.463, 0.654, 0.925, 1.309, 1.851, 2.618, 3.702, 5.235, 7.404, 10.470, 14.807, 20.941, 29.615, 41.882, 59.230, 83.763) mJy. Optical levels are (0.087, 0.123, 0.174, 0.246, 0.349, 0.493, 0.698, 0.987, 1.396, 1.974, 2.792, 3.949) $\times 10^{-14}$ ergs s^{-1} arcsec^{-2}. The radio map courtesy of D. Floyd (2006, private communication).

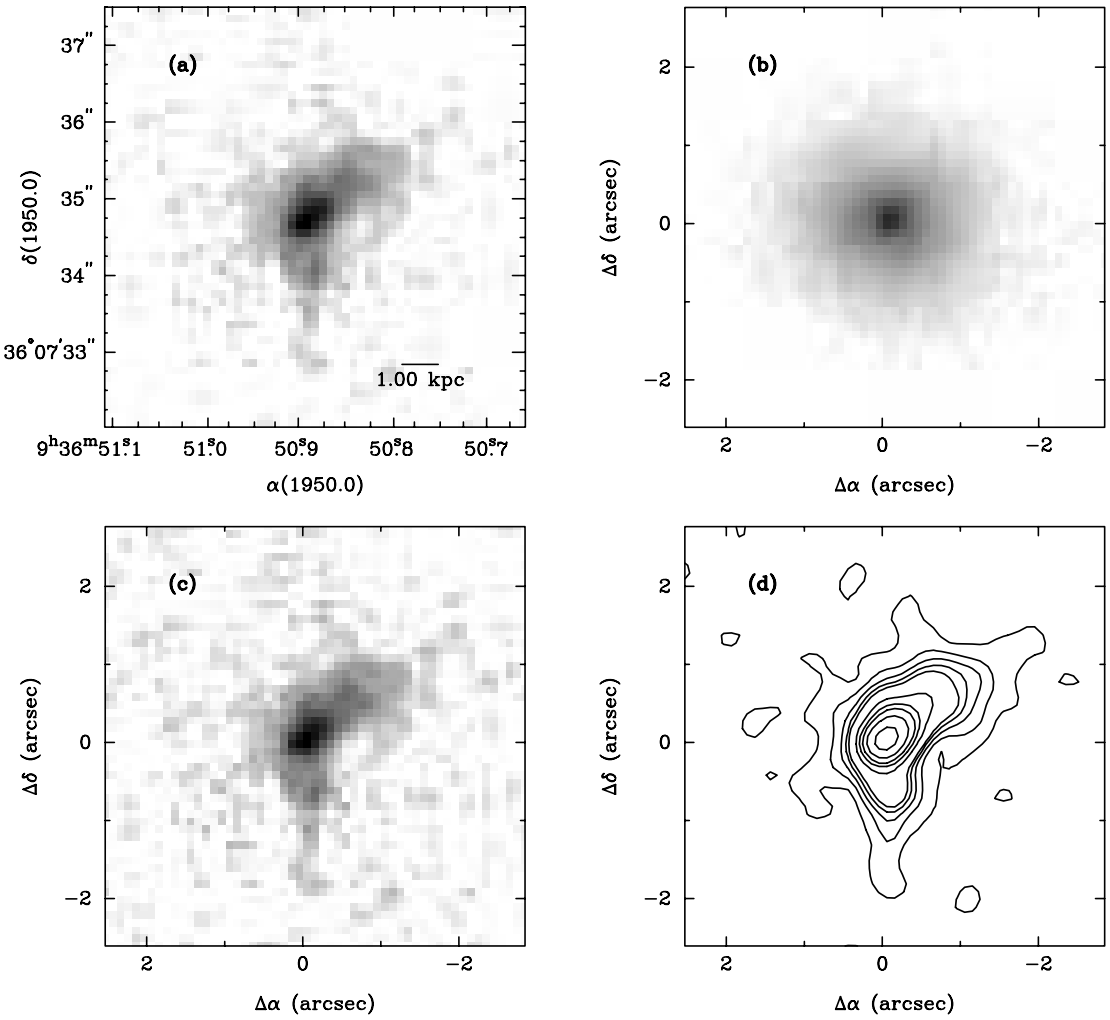

FIG. 25.—3C 223 (optical montage). Starting at the top left, going clockwise: LRF image, broadband image, continuum-subtracted image (*contours*), and continuum-subtracted image (*gray scale*).

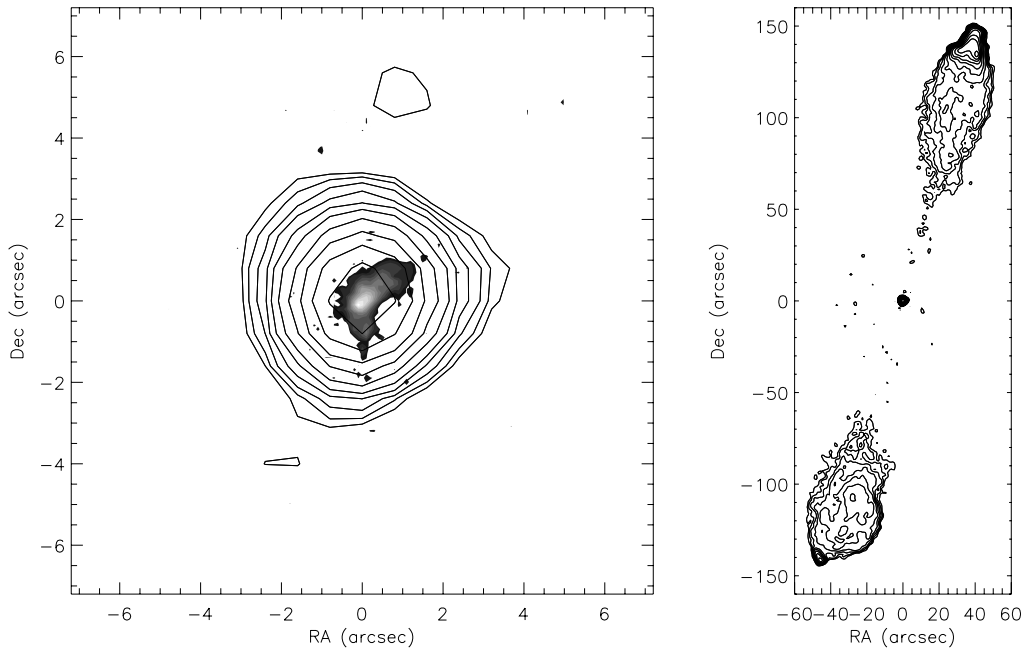

FIG. 26.—3C 223 (radio/optical overlay). Radio is shown in contours. Optical is shown in gray scale. *Left*: Close-up of the core. *Right*: View of the overall radio source. Radio levels are (0.258, 0.365, 0.516, 0.730, 1.032, 1.459, 2.064, 2.919, 4.128, 5.838, 8.256) mJy. Optical levels are (0.168, 0.237, 0.336, 0.475, 0.672, 0.950, 1.344, 1.901, 2.688, 3.802, 5.377, 7.605, 10.755) $\times 10^{-14}$ ergs s^{-1} arcsec^{-2}. Both images have the same levels. The radio map courtesy of D. Floyd (2006, private communication).

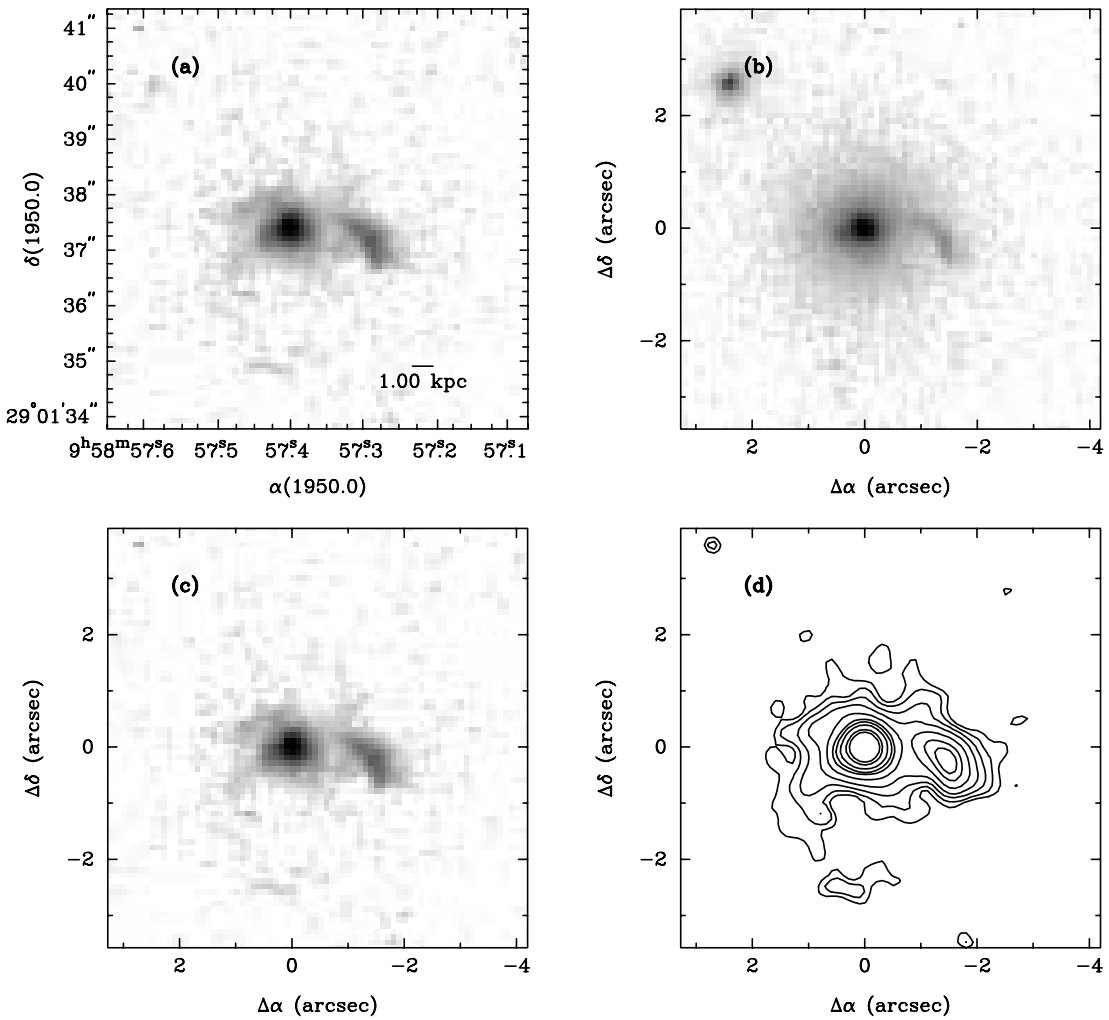

FIG. 27.—3C 234 (optical montage). Starting at the top left, going clockwise: LRF image, broadband image, continuum-subtracted image (*contours*), and continuum-subtracted image (*gray scale*).

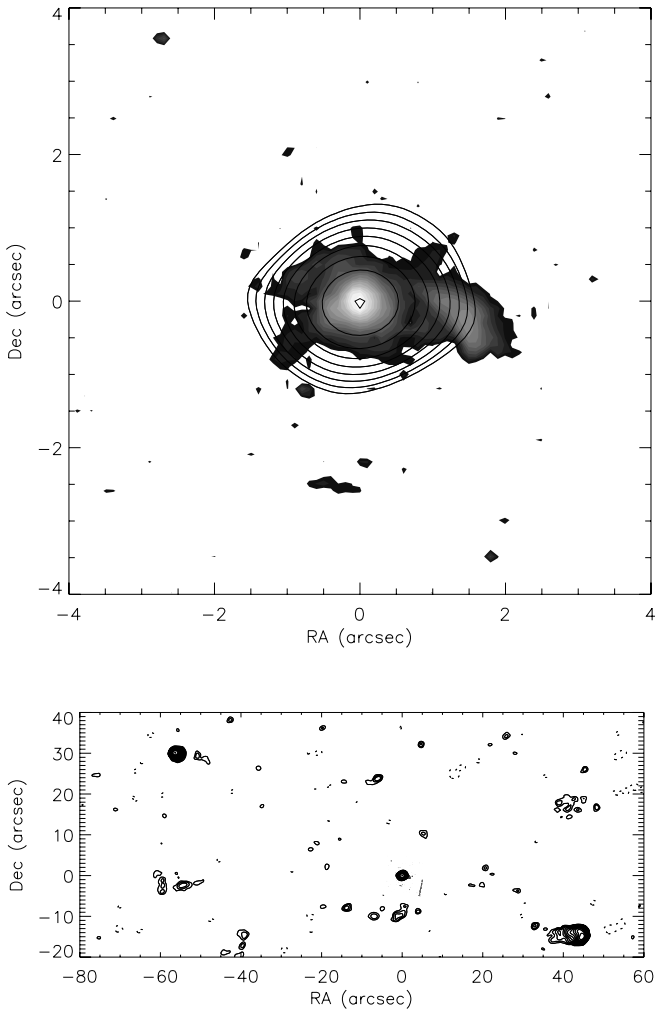

FIG. 28.—3C 234 (radio/optical overlay). Radio is shown in contours. Optical is shown in gray scale. *Top*: Close-up of the core. *Bottom*: View of the overall radio source. Radio levels are (2.226, 3.148, 4.451, 6.295, 8.903, 12.590, 17.806, 25.181, 35.611, 50.362, 71.222, 100.724, 142.445, 201.447, 284.890, 402.895, 569.779) mJy. Optical levels are (0.224, 0.317, 0.448, 0.634, 0.897, 1.269, 1.795, 2.538, 3.590, 5.077, 7.181, 10.155, 14.362, 20.311, 28.724, 40.622, 57.448) $\times 10^{-14}$ ergs s^{-1} $arcsec^{-2}$. Both images have the same levels. Radio map from Neff et al. (1995).

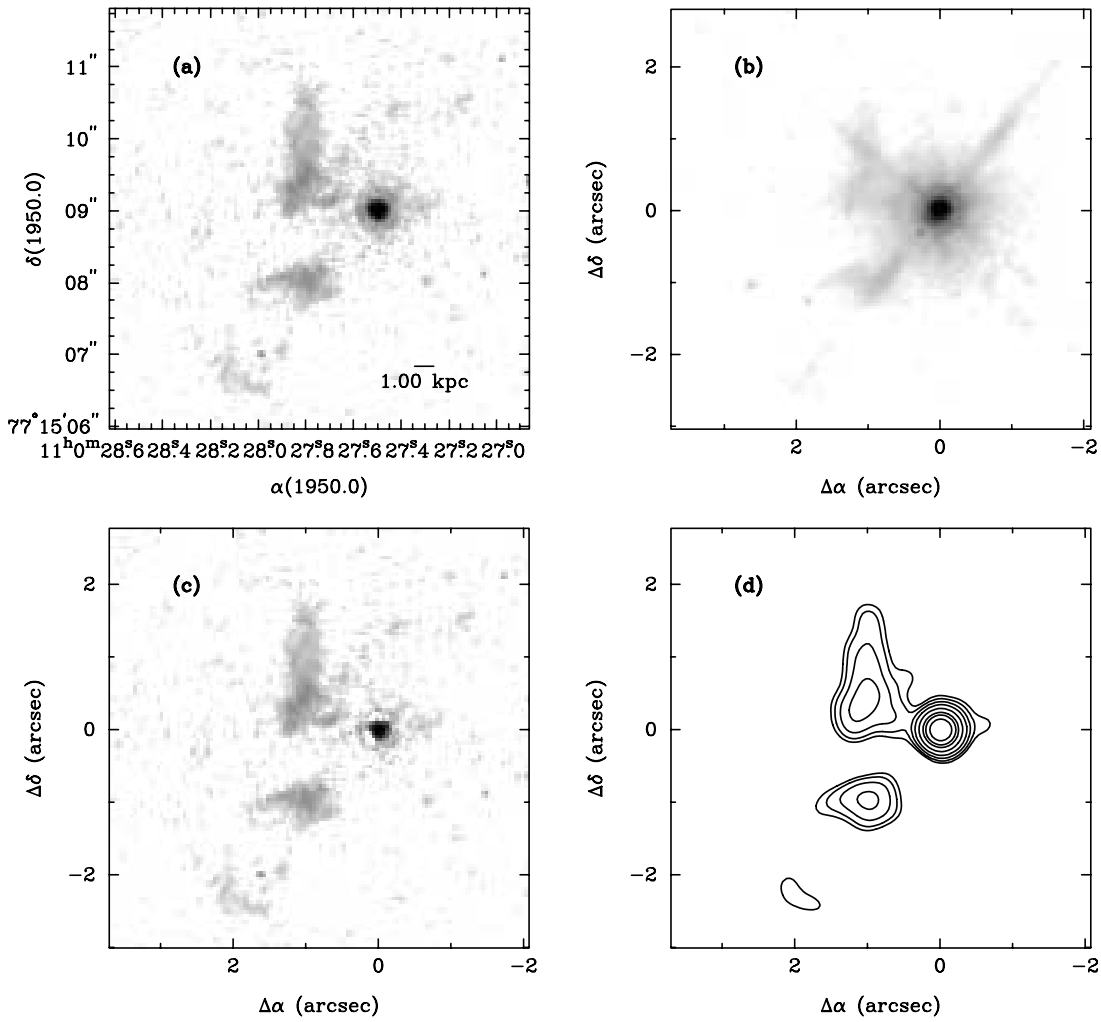

FIG. 29.—3C 249.1 (optical montage). Starting at the top left, going clockwise: LRF image, broadband image, continuum-subtracted image (*contours*), and continuum-subtracted image (*gray scale*).

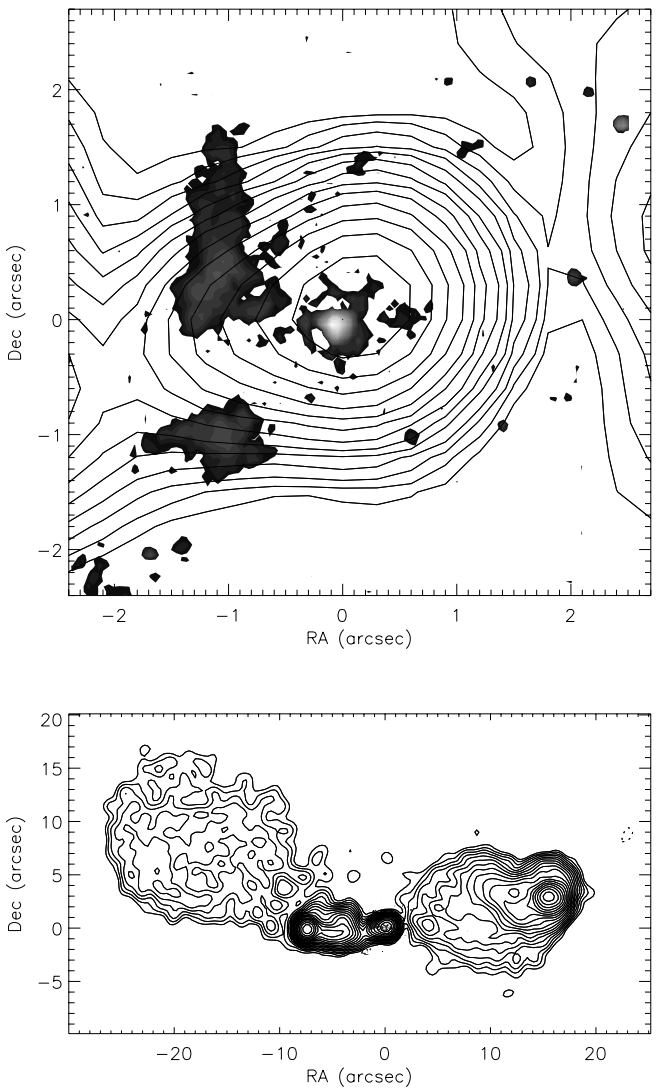

FIG. 30.—3C 249.1 (radio/optical overlay). Radio is shown in contours. Optical is shown in gray scale. *Top*: Close-up of the core. *Bottom*: View of the overall radio source. Radio levels are (0.674, 0.953, 1.348, 1.907, 2.696, 3.813, 5.393, 7.627, 10.786, 15.253, 21.571, 30.506, 43.142, 61.013, 86.285, 122.025, 172.570, 244.050) mJy. Optical levels are (0.306, 0.433, 0.613, 0.867, 1.226, 1.734, 2.453, 3.469, 4.906, 6.938, 55.507, 78.499, 111.014, 156.998) $\times 10^{-14}$ ergs s^{-1} arcsec^{-2}. Both images have the same levels. Radio map from J. P. Laing (image obtained from the 3CRR Atlas; http://www.jb.man.ac.uk/atlas).

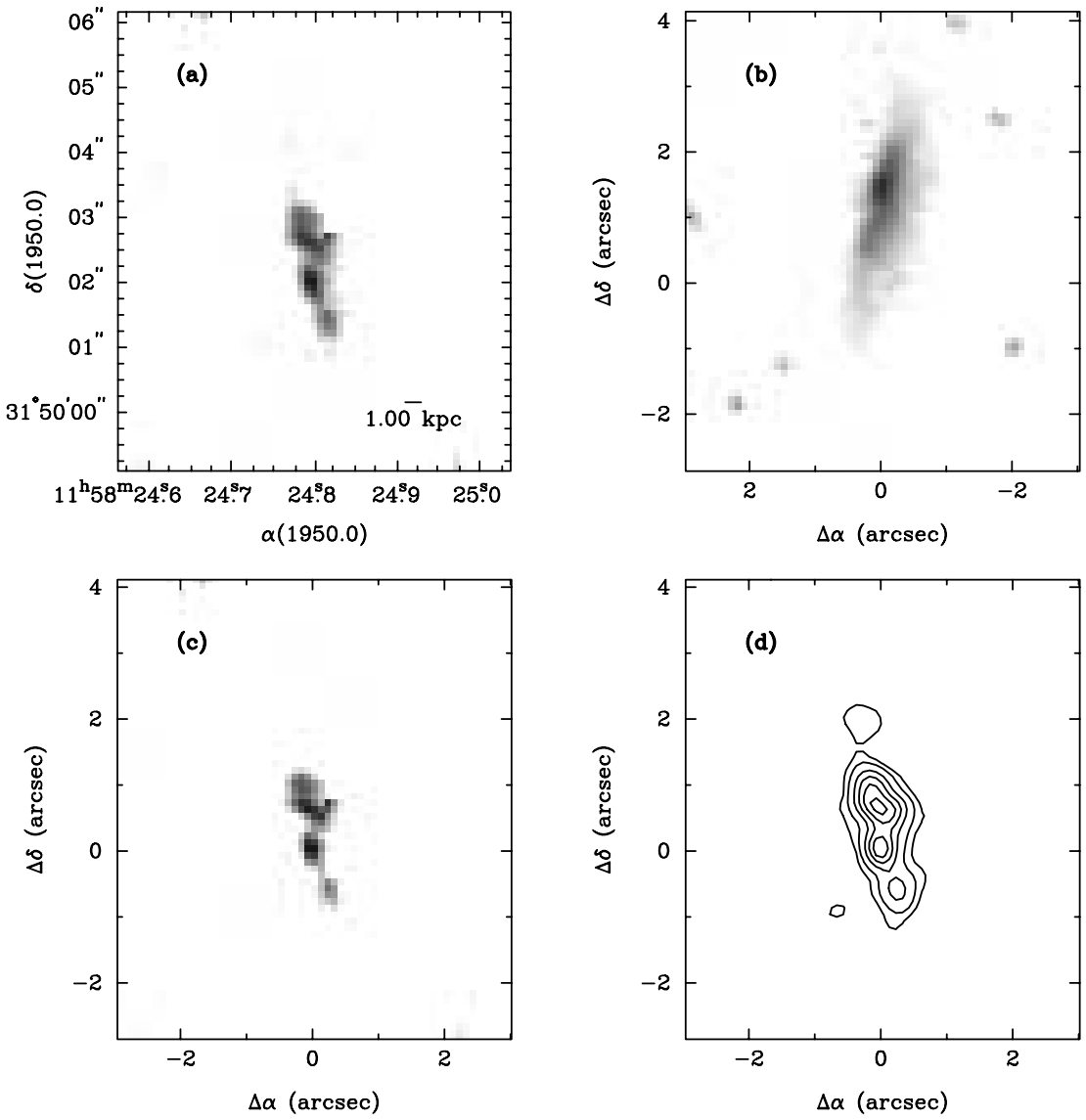

FIG. 31.—3C 268.2 (optical montage). Starting at the top left, going clockwise: LRF image, broadband image, continuum-subtracted image (*contours*), and continuum-subtracted image (*gray scale*).

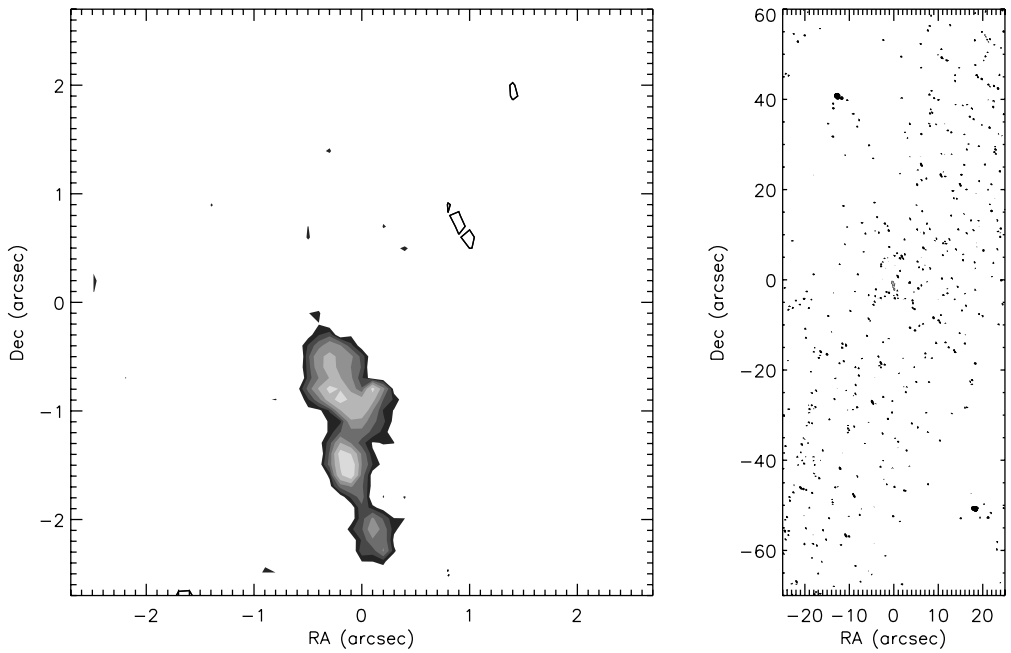

FIG. 32.—3C 268.2 (radio/optical overlay). Radio is shown in contours. Optical is shown in gray scale. *Left*: Close-up of the core. *Right*: View of the overall radio source. Radio levels are (1.212, 1.714, 2.424, 3.428, 4.848, 6.856, 9.696, 13.712) mJy. Optical levels are (0.104, 0.148, 0.209, 0.296, 0.418, 0.592, 0.837) $\times 10^{-14}$ ergs s^{-1} arcsec^{-2}. Both images have the same levels. The radio map is from Neff et al. (1995).

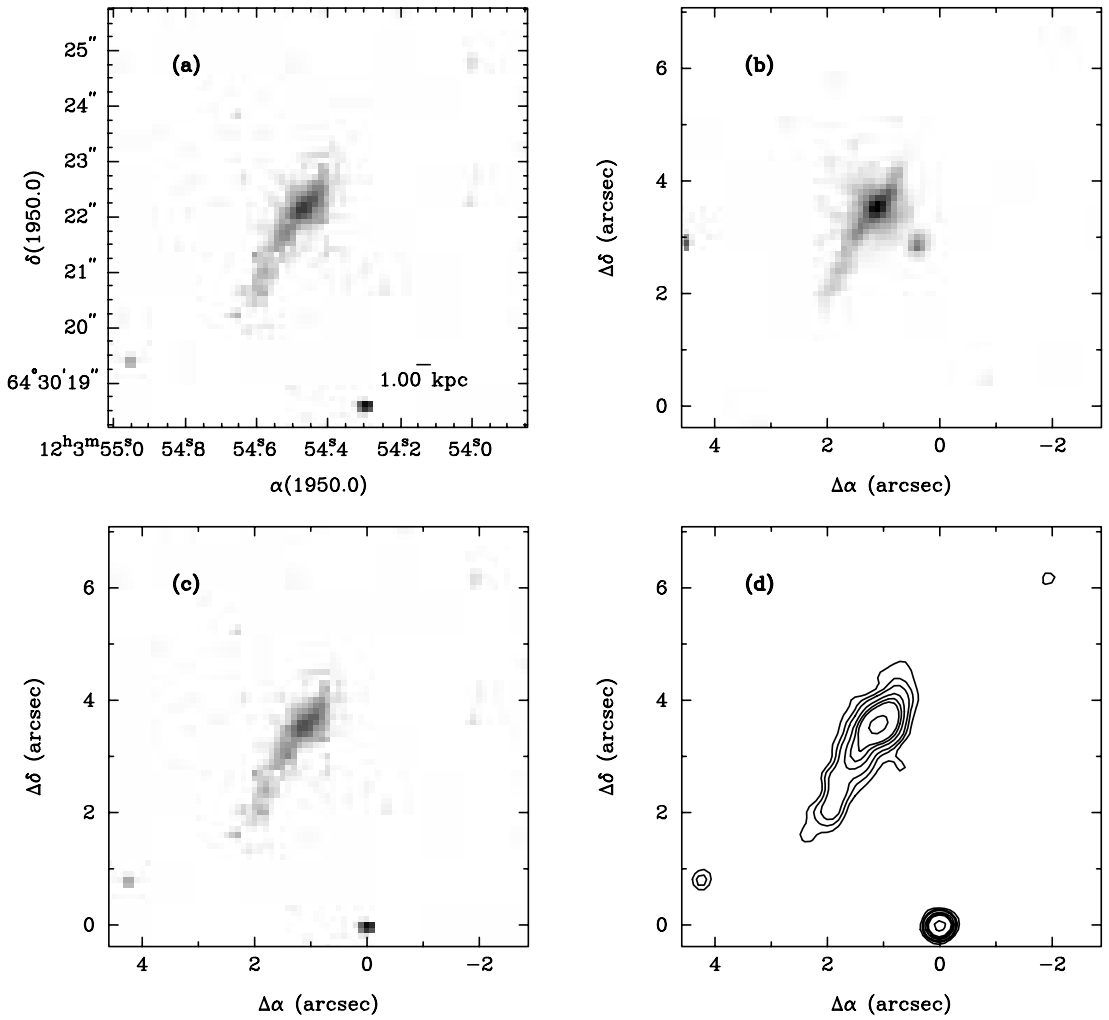

FIG. 33.—3C 268.3 (optical montage). Starting at the top left, going clockwise: LRF image, broadband image, continuum-subtracted image (*contours*), and continuum-subtracted image (*gray scale*).

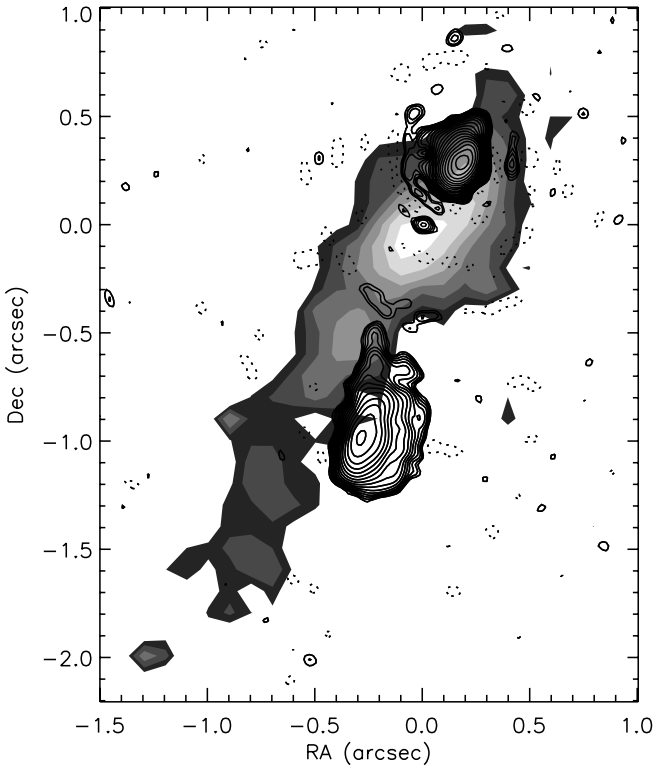

FIG. 34.—3C 268.3 (radio/optical overlay). Radio is shown in contours. Optical is shown in gray scale. Radio levels are (0.193, 0.272, 0.385, 0.545, 0.770, 1.090, 1.541, 2.179, 3.082, 4.358, 6.163, 8.716, 12.326, 17.432, 24.653, 34.864, 49.306, 69.729, 98.611, 139.457) mJy. Optical levels are (0.0865, 0.1223, 0.1731, 0.2448, 0.3461, 0.4896, 0.6923) $\times 10^{-14}$ ergs s^{-1} arcsec^{-2}. The radio map is from Ludke et al. (1998).

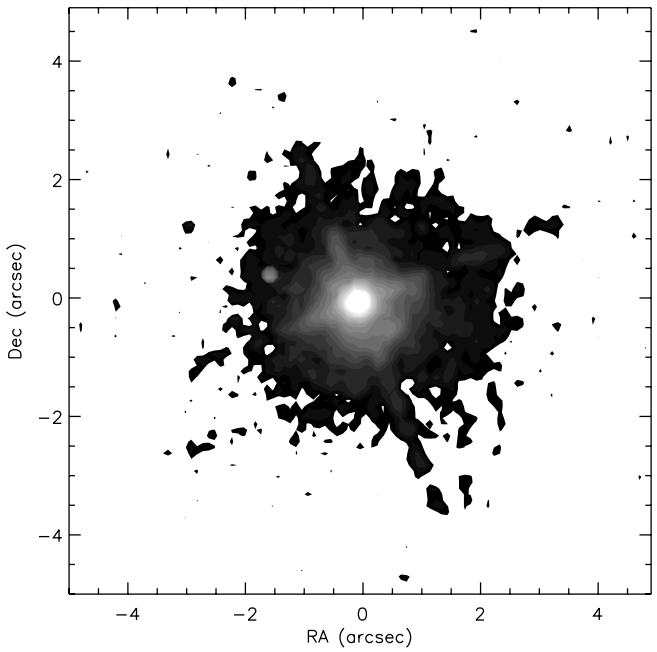

FIG. 35.—3C 273 (narrowband image). Optical levels are (0.184, 0.261, 0.369, 0.522, 0.738, 1.044, 1.476, 2.088, 2.953, 4.177, 5.907, 8.354, 11.814, 16.708, 23.629, 33.416, 47.258, 66.833, 94.517, 133.667) $\times 10^{-14}$ ergs s^{-1} arcsec^{-2}.

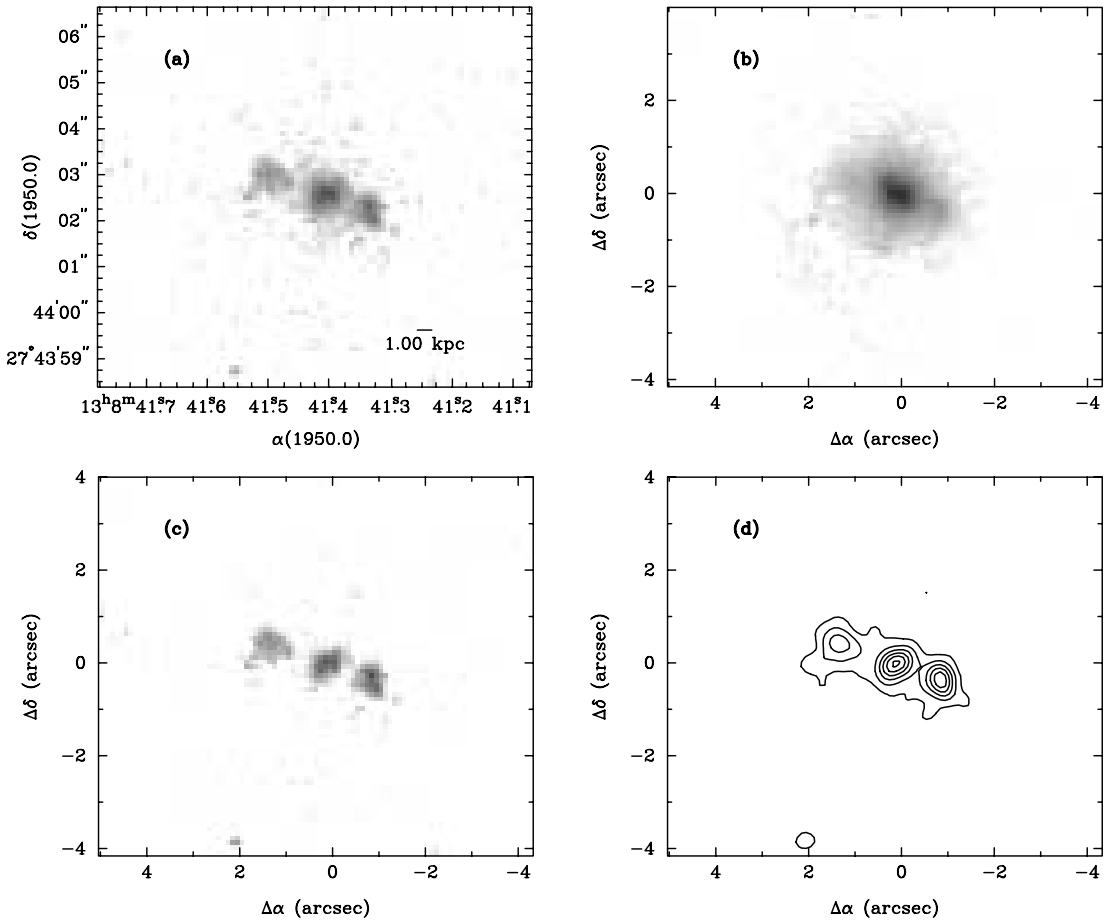

FIG. 36.—3C 284 (optical montage). Starting at the top left, going clockwise: LRF image, broadband image, continuum-subtracted image (*contours*), and continuum-subtracted image (*gray scale*).

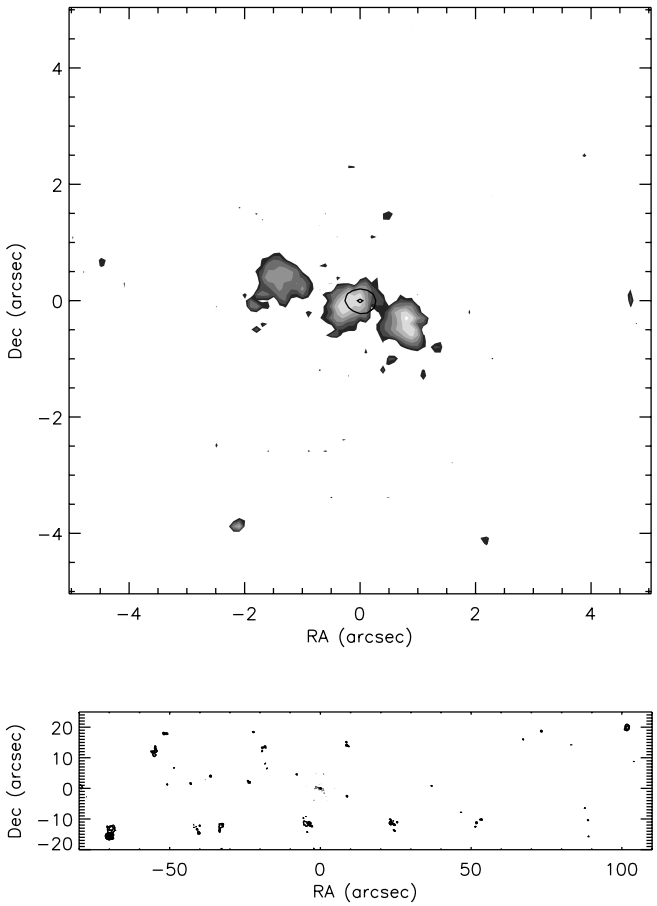

FIG. 37.—3C 284 (radio/optical overlay). Radio is shown in contours. Optical is shown in gray scale. *Top*: Close-up of the core. *Bottom*: View of the overall radio source. Radio levels are (1.796, 2.540, 3.593, 5.081, 7.186, 10.162, 14.371, 20.324, 28.742) mJy. Optical levels are (0.081, 0.115, 0.163, 0.231, 0.327, 0.463, 0.655) × 10^{-14} ergs s^{-1} $arcsec^{-2}$. Both images have the same levels.

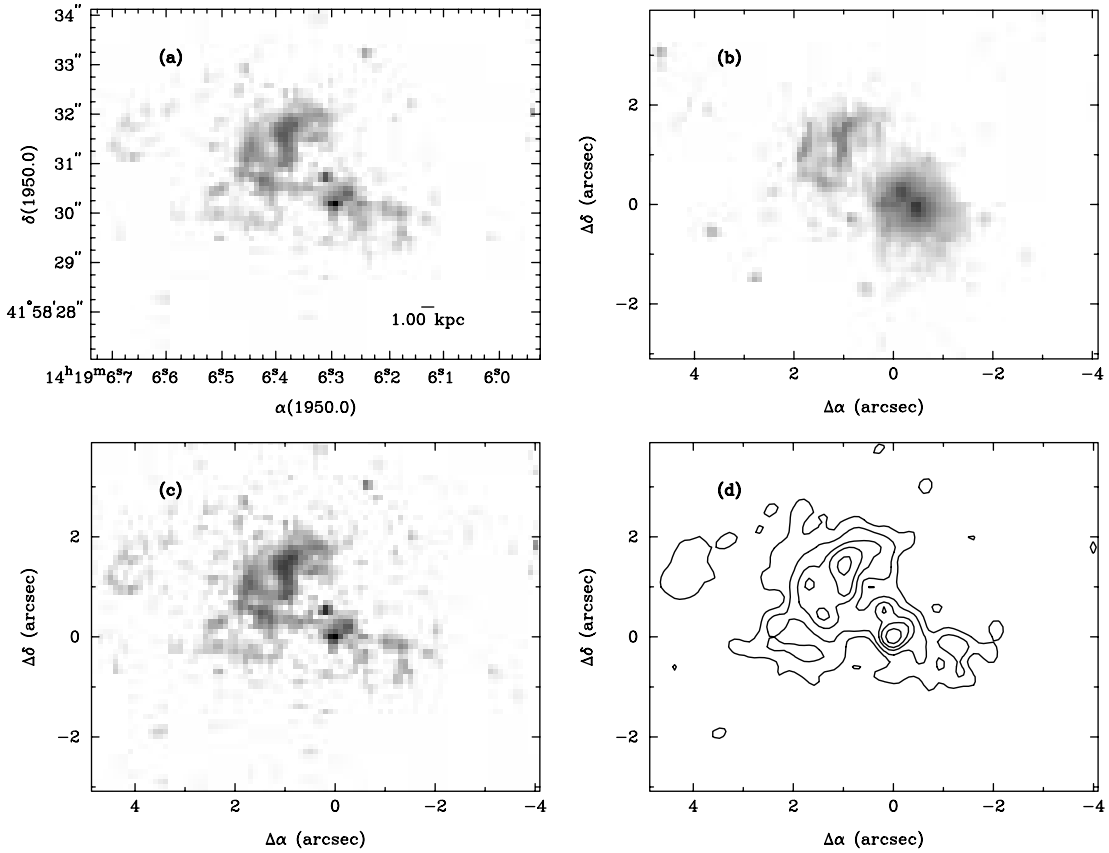

FIG. 38.—3C 299 (optical montage). Starting at the top left, going clockwise: LRF image, broadband image, continuum-subtracted image (*contours*), and continuum-subtracted image (*gray scale*).

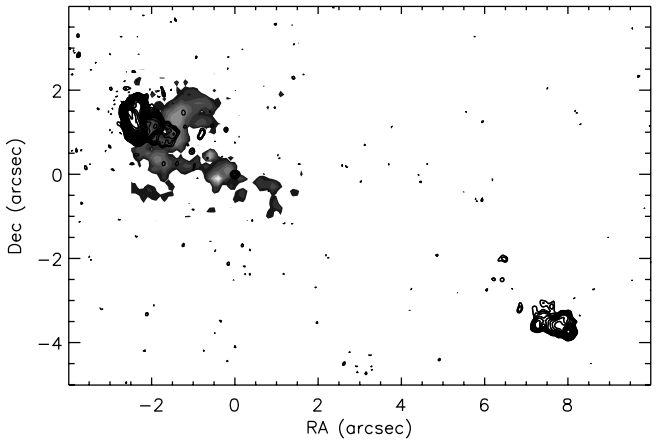

FIG. 39.—3C 299 (radio/optical overlay). Radio is shown in contours. Optical is shown in gray scale. Radio levels are (0.430, 0.608, 0.860, 1.216, 1.720, 2.432, 3.439, 4.864, 6.878, 9.728, 13.757, 19.455, 27.514, 38.910, 55.027, 77.820, 110.054, 155.640, 220.109, 311.281) mJy. Optical levels are (0.087, 0.123, 0.175, 0.247, 0.350, 0.495, 0.701, 0.991, 1.401, 1.982, 2.803) $\times 10^{-14}$ ergs s^{-1} arcsec^{-2}. The radio map was provided by J. P. Laing (image obtained from the 3CRR Atlas; http://www.jb.man.ac.uk/atlas).

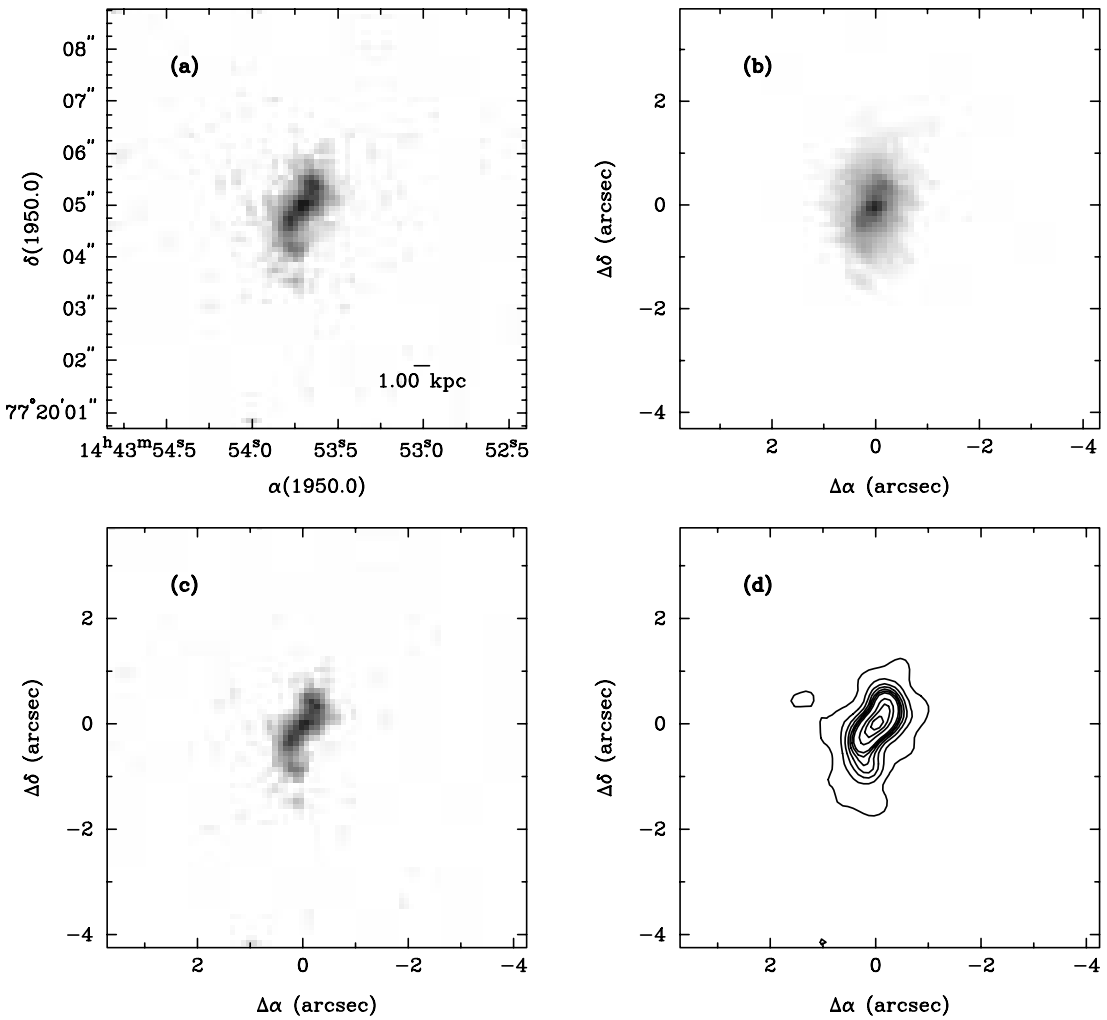

FIG. 40.—3C 303.1 (optical montage). Starting at the top left, going clockwise: LRF image, broadband image, continuum-subtracted image (*contours*), and continuum-subtracted image (*gray scale*).

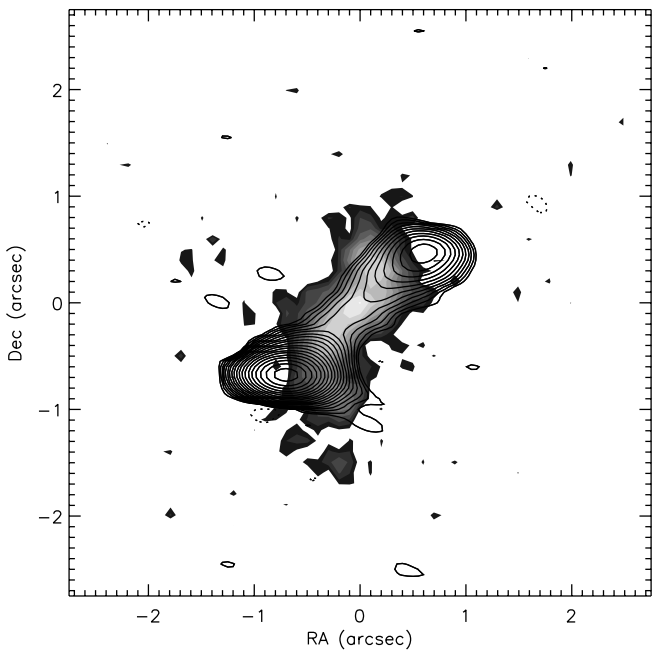

FIG. 41.—3C 303.1 (radio/optical overlay). Radio is shown in contours. Optical is shown in gray scale. Radio levels are (0.228, 0.322, 0.455, 0.644, 0.910, 1.288, 1.821, 2.575, 3.642, 5.150, 7.283, 10.300, 14.566, 20.600, 29.133, 41.200, 58.266, 82.400, 116.531) mJy. Optical levels are (0.077, 0.109, 0.154, 0.218, 0.308, 0.436, 0.617, 0.872, 1.234, 1.745, 2.468) $\times 10^{-14}$ ergs s^{-1} arcsec^{-2}.

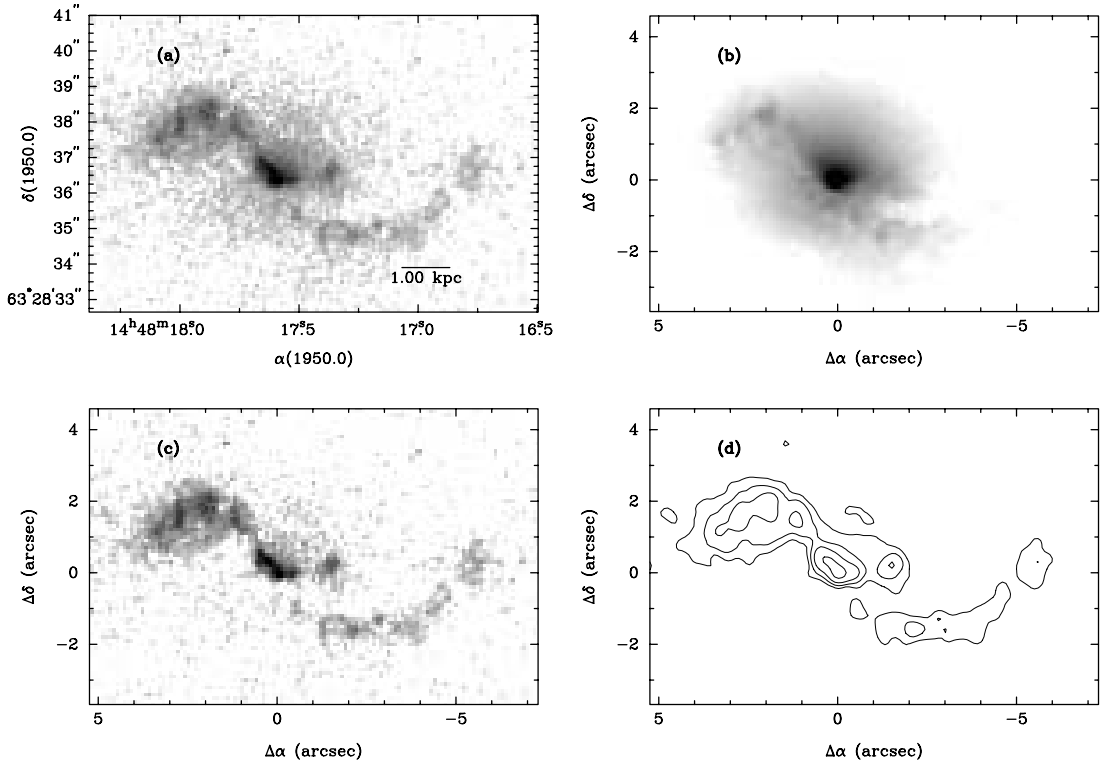

FIG. 42.—3C 305 (optical montage). Starting at the top left, going clockwise: LRF image, broadband image, continuum-subtracted image (*contours*), and continuum-subtracted image (*gray scale*).

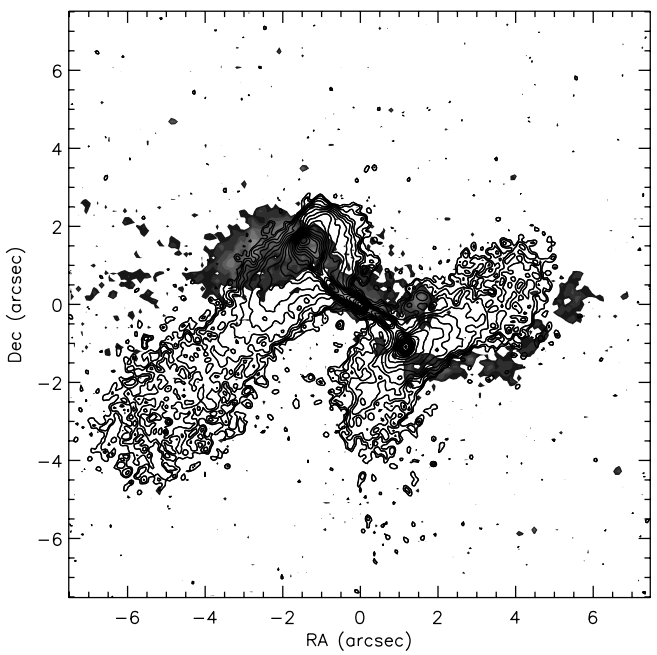

FIG. 43.—3C 305 (radio/optical overlay). Radio is shown in contours. Optical is shown in gray scale. Radio levels are (0.236, 0.334, 0.473, 0.669, 0.946, 1.337, 1.891, 2.675, 3.782, 5.349, 7.565, 10.698, 15.130, 21.396, 30.259, 42.793, 60.518, 85.586) mJy. Optical levels are (0.277, 0.392, 0.554, 0.784, 1.108, 1.568, 2.217, 3.136, 4.435, 6.272, 8.870) $\times 10^{-14}$ ergs s^{-1} arcsec^{-2}. The radio map was provided by J. P. Laing (image obtained from the 3CRR Atlas; http://www.jb.man.ac.uk/atlas).

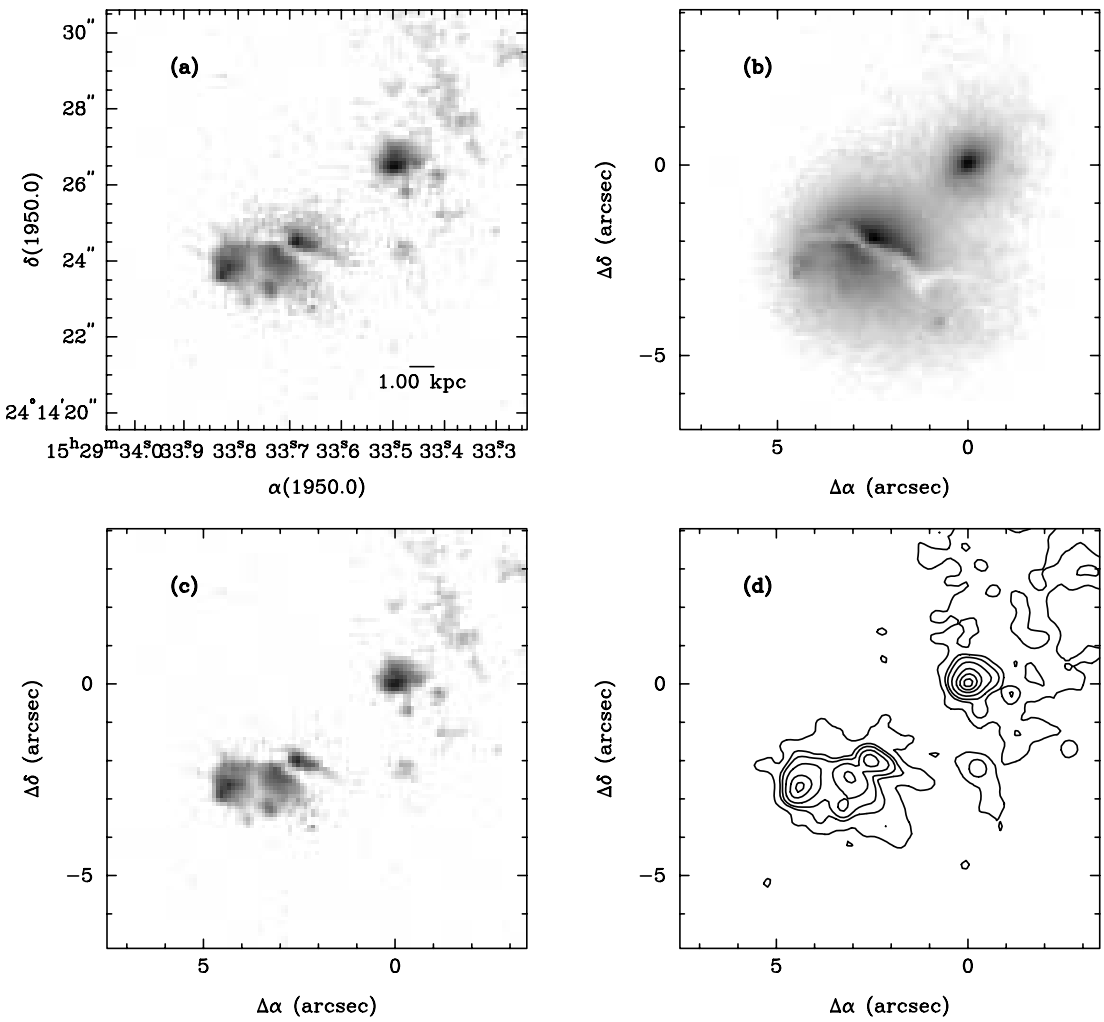

FIG. 44.—3C 321 (optical montage). Starting at the top left, going clockwise: LRF image, broadband image, continuum-subtracted image (*contours*), and continuum-subtracted image (*gray scale*).

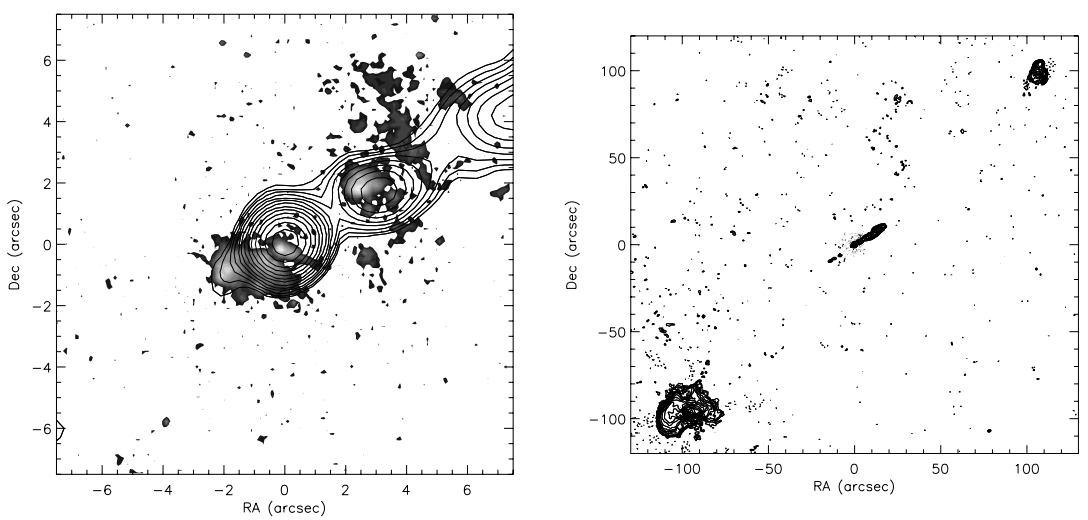

FIG. 45.—3C 321 (radio/optical overlay). Radio is shown in contours. Optical is shown in gray scale. *Left*: Close-up of the core. *Right*: View of the overall radio source. Radio levels are (0.368, 0.520, 0.736, 1.040, 1.471, 2.081, 2.942, 4.161, 5.885, 8.322, 11.770, 16.645, 23.539, 33.289, 47.078, 66.579, 94.157, 133.158, 188.314, 266.316) mJy. Optical levels are (0.135, 0.190, 0.270, 0.381, 0.388, 0.763, 1.079, 1.527, 2.159, 3.054, 4.319, 6.108) $\times 10^{-14}$ ergs s^{-1} arcsec^{-2}. Both images have the same levels. The radio map was provided courtesy of D. Floyd (2006, private communication).

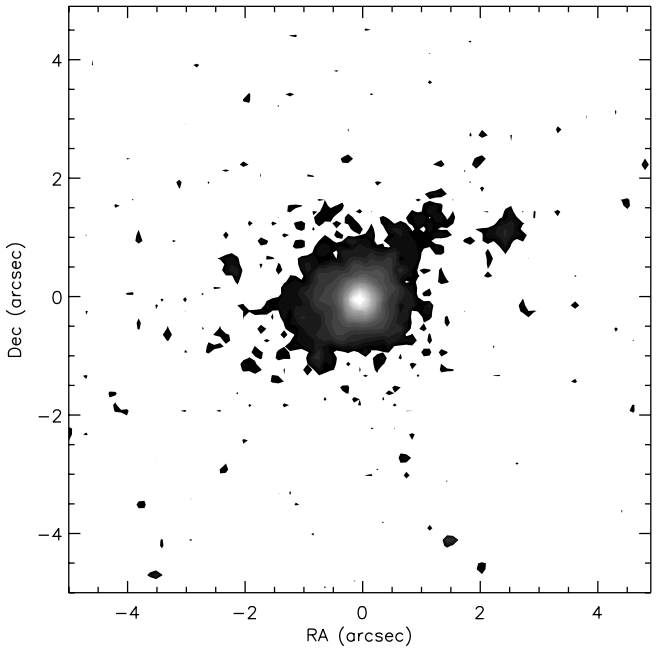

FIG. 46.—3C 323.1 (narrowband image). Optical levels are (0.156, 0.221, 0.313, 0.443, 0.627, 0.887, 1.254, 1.773, 2.508, 3.547, 5.017, 7.095, 10.034, 14.191, 20.069, 28.382, 40.138, 56.763, 80.276, 113.528) $\times 10^{-14}$ ergs s^{-1} arcsec^{-2}.

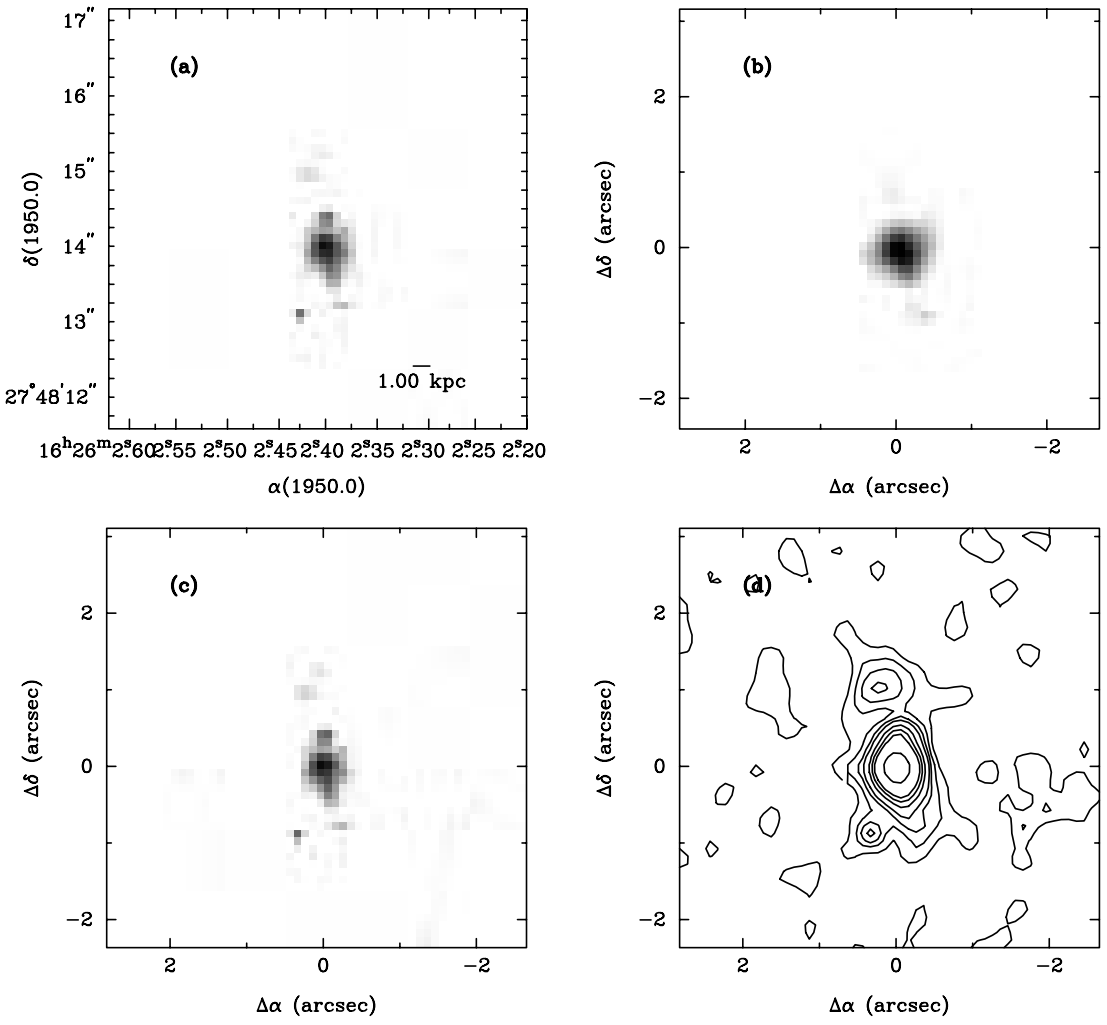

FIG. 47.—3C 341 (optical montage). Starting at the top left, going clockwise: LRF image, broadband image, continuum-subtracted image (*contours*), and continuum-subtracted image (*gray scale*).

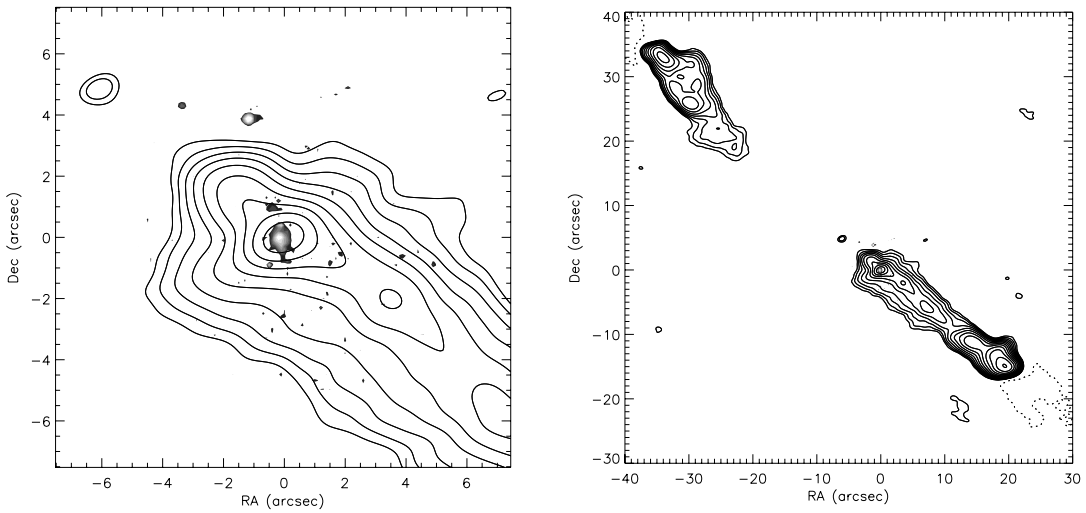

FIG. 48.—3C 341 (radio/optical overlay). Radio is shown in contours. Optical is shown in gray scale. *Left*: Close-up of the core. *Right*: View of the overall radio source. Radio levels are (0.288, 0.407, 0.576, 0.815, 1.152, 1.629, 2.304, 3.258, 4.608, 6.517, 9.216, 13.033) mJy. Optical levels are (0.096, 0.136, 0.193, 0.273, 0.386, 0.546, 0.772, 1.093) $\times 10^{-14}$ ergs s^{-1} arcsec^{-2}. Both images have the same levels.

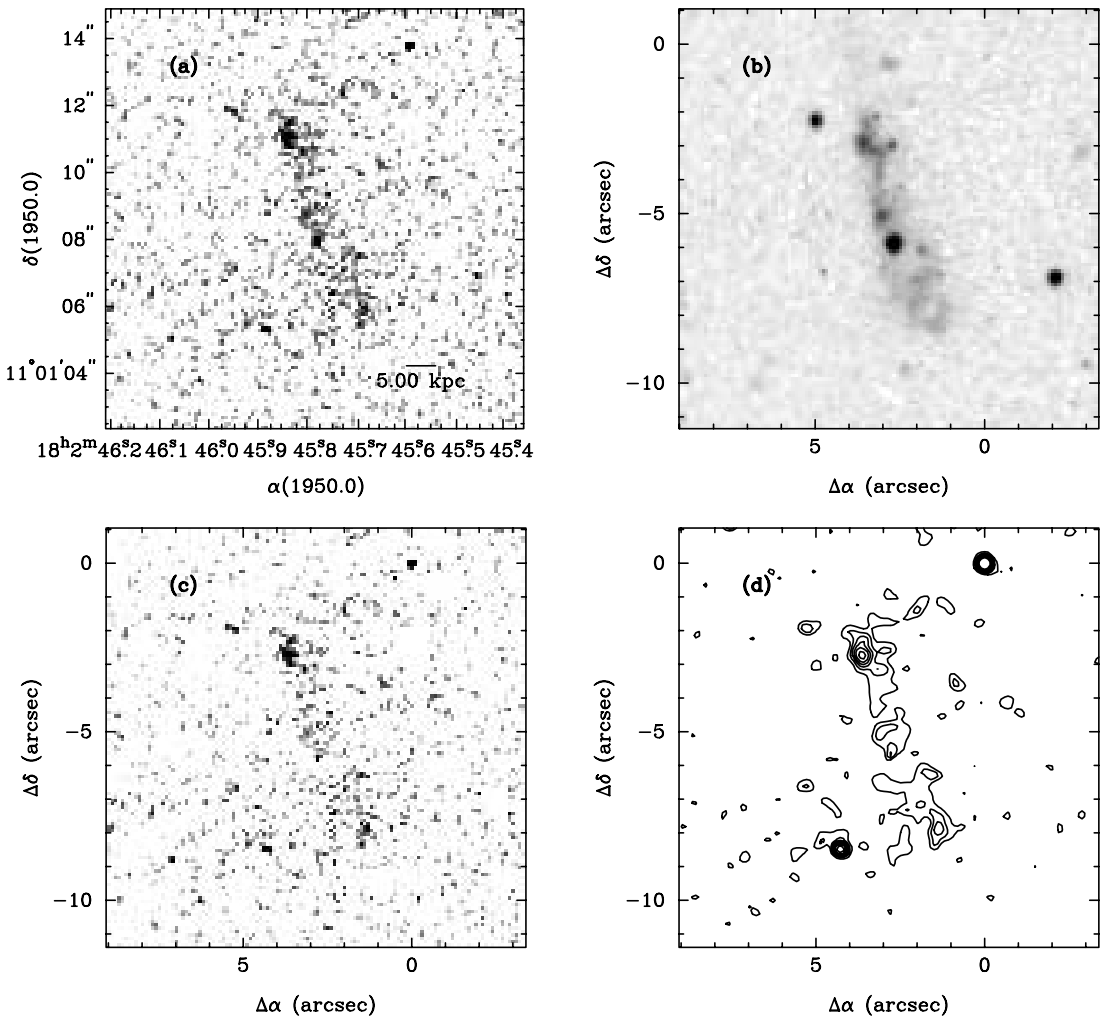

FIG. 49.—3C 368 (optical montage). Starting at the top left, going clockwise: LRF image, broadband image, continuum-subtracted image (*contours*), and continuum-subtracted image (*gray scale*).

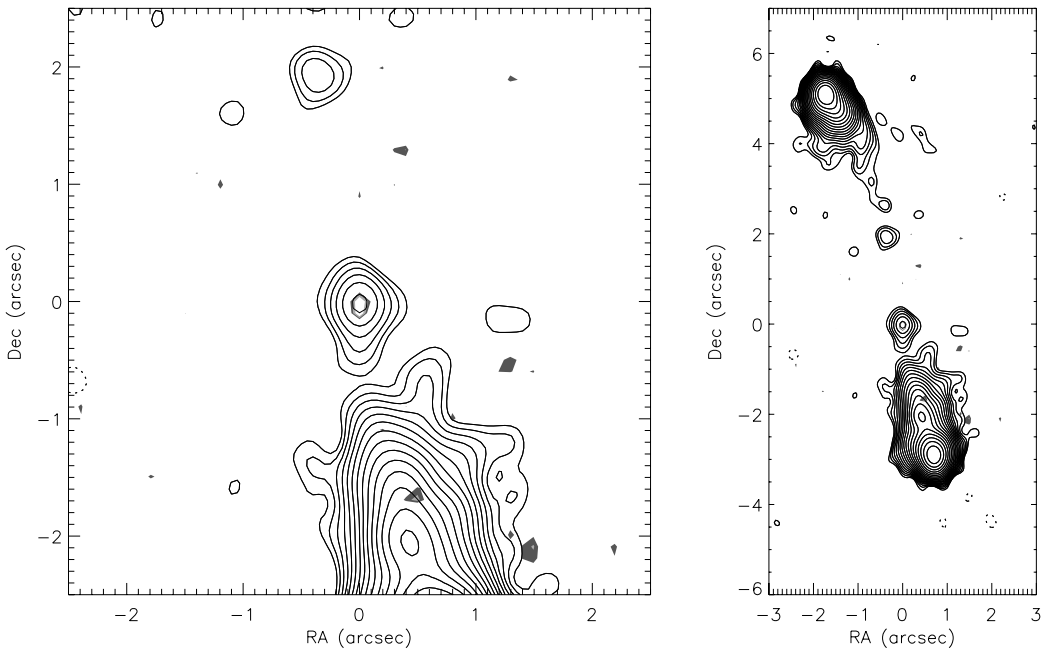

FIG. 50.—3C 368 (radio/optical overlay). Radio is shown in contours. Optical is shown in gray scale. *Left*: Close-up of the core. *Right*: View of the overall radio source. Radio levels are (0.098, 0.138, 0.195, 0.276, 0.391, 0.553, 0.782, 1.105, 1.563, 2.211, 3.126, 4.421, 6.253, 8.843, 12.506, 17.686, 25.011, 35.371) mJy. Optical levels are (0.114, 0.162, 0.229) $\times 10^{-14}$ ergs s^{-1} arcsec^{-2}. Both images have the same levels.

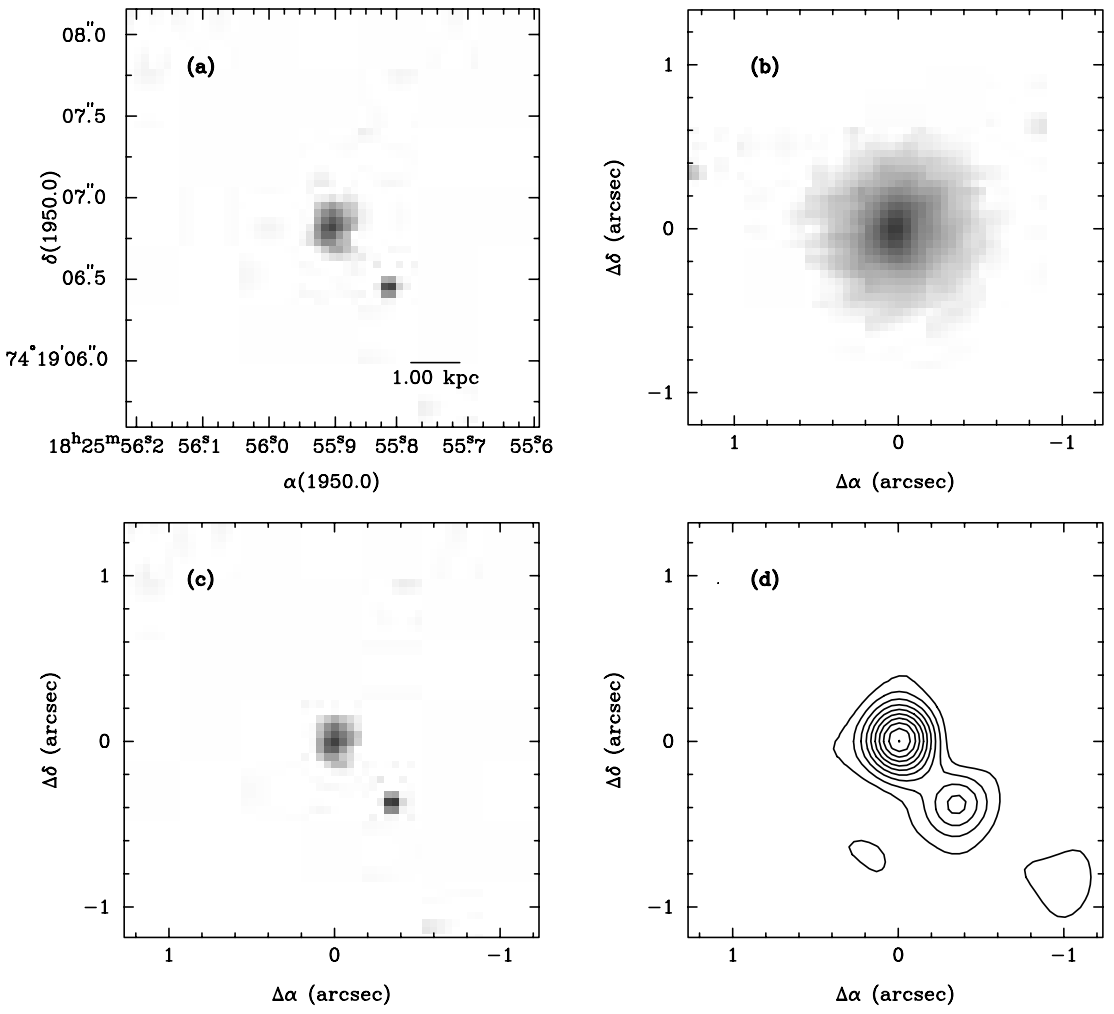

FIG. 51.—3C 379.1 (optical montage). Starting at the top left, going clockwise: LRF image, broadband image, continuum-subtracted image (*contours*), and continuum-subtracted image (*gray scale*).

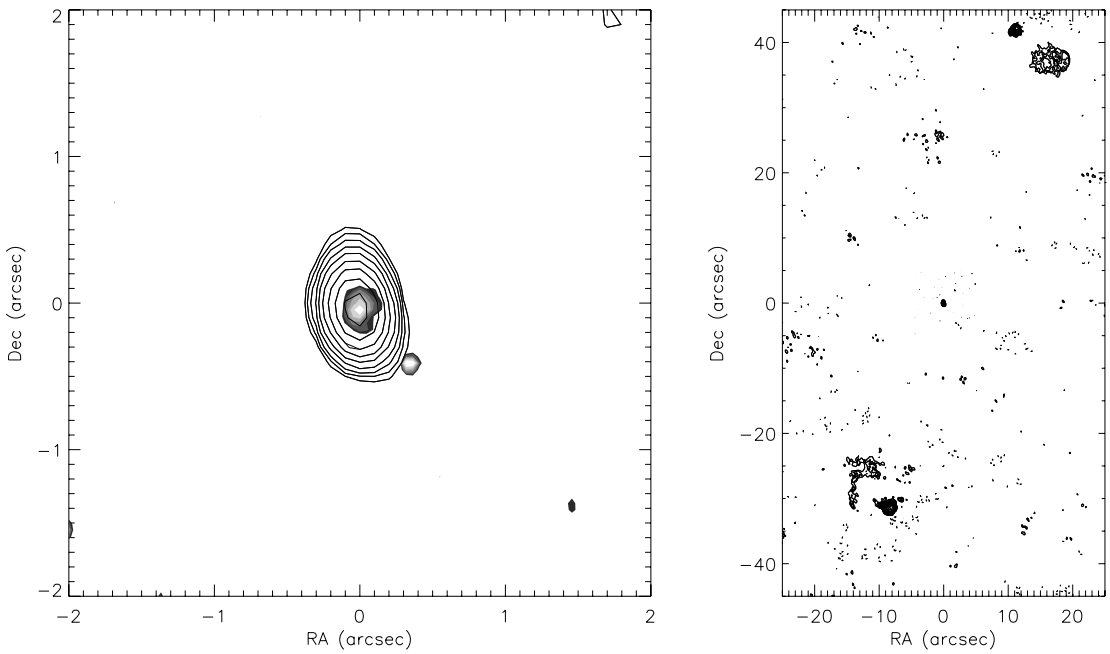

FIG. 52.—3C 379.1 (radio/optical overlay). Radio is shown in contours. Optical is shown in gray scale. *Left*: Close-up of the core. *Right*: View of the overall radio source. Radio levels are (0.225, 0.318, 0.449, 0.635, 0.898, 1.271, 1.797, 2.541, 3.594, 5.082, 7.187, 10.164, 14.374, 20.328) mJy. Optical levels are (0.311, 0.440, 0.622, 0.880, 1.245, 1.761) $\times 10^{-14}$ ergs s^{-1} arcsec^{-2}. Both images have the same levels.

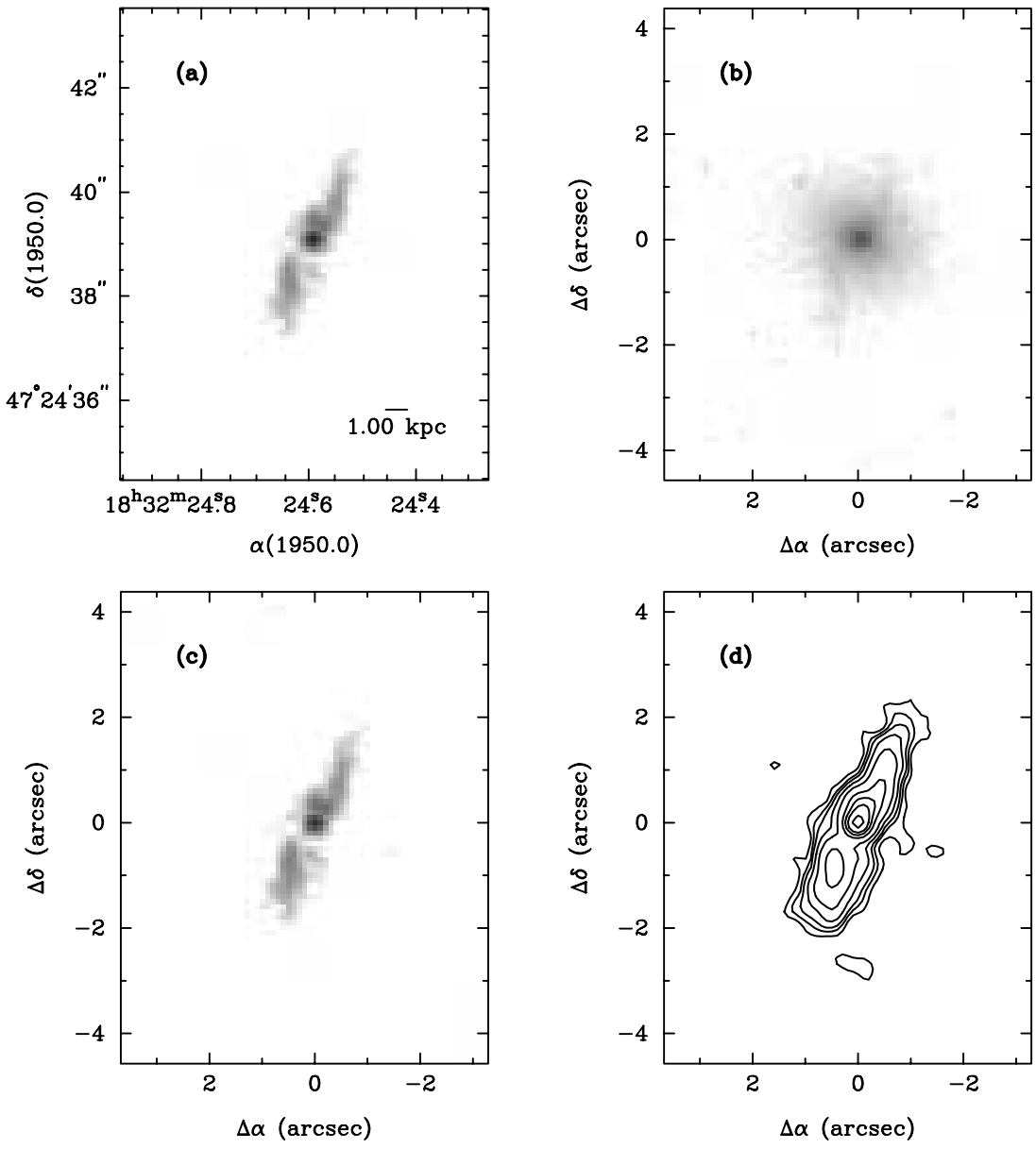

FIG. 53.—3C 381 (optical montage). Starting at the top left, going clockwise: LRF image, broadband image, continuum-subtracted image (*contours*), and continuum-subtracted image (*gray scale*).

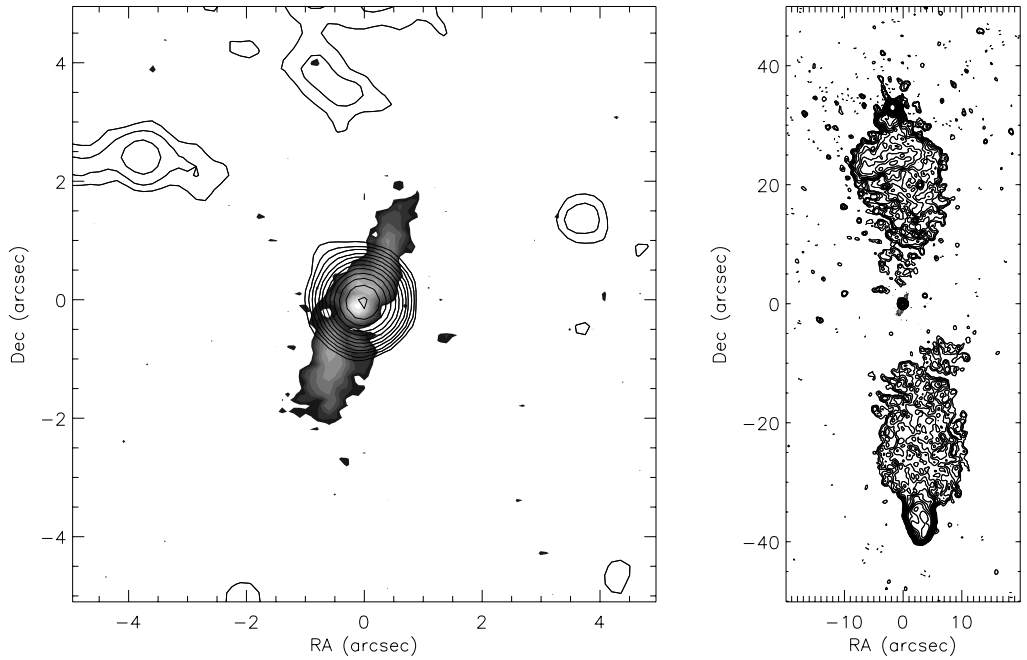

FIG. 54.—3C 381 (radio/optical overlay). Radio is shown in contours. Optical is shown in gray scale. *Left*: Close-up of the core. *Right*: View of the overall radio source. Radio levels are (0.102, 0.144, 0.203, 0.288, 0.407, 0.575, 0.814, 1.151, 1.627, 2.301, 3.254, 4.602, 6.509, 9.205, 13.018, 18.410, 26.035, 36.819, 52.070, 73.639) mJy. Optical levels are (0.146, 0.207, 0.292, 0.414, 0.585, 0.828, 1.171, 1.656, 2.342, 3.312, 4.685) $\times 10^{-14}$ ergs s^{-1} arcsec^{-2}. Both images have the same levels. The radio map was provided by D. Floyd (2006, private communication).

REFERENCES

Akujor, C. E., & Garrington, S. T. 1995, A&AS, 112, 235
Allington-Smith, J. R. 1984, MNRAS, 210, 611
Antonucci, R. R. J. 1984, ApJ, 278, 499
Axon, D. J., Capetti, A., Fanti, R., Morganti, R., Robinson, A., & Spencer, R. 2000, AJ, 120, 2284
Baum, S. A., & Heckman, T. 1989a, ApJ, 336, 681
———. 1989b, ApJ, 336, 702
Baum, S. A., Heckman, T. M., Bridle, A., van Breugel, W. J. M., & Miley, G. K. 1988, ApJS, 68, 643
Bennett, A. S. 1962, MmRAS, 68, 163
Best, P. N., Röttgering, H. J. A., & Longair, M. S. 2000, MNRAS, 311, 23
Biretta, J. A. 1996, WFPC2 Instrument Handbook (Baltimore: STScI)
Biretta, J. A., Martel, A. R., McMaster, M., Sparks, W. B., Baum, S. A., Macchetto, F., & McCarthy, P. J. 2002, NewA Rev., 46, 181
Chambers, K. C., Miley, G. K., & van Breugel, W. 1987, Nature, 329, 604
Dallacasa, D., Fanti, C., Fanti, R., Schilizzi, R. T., & Spencer, R. E. 1995, A&A, 295, 27
de Koff, S., Baum, S. A., Sparks, W. B., Biretta, J., Golombek, D., Macchetto, F., McCarthy, P., & Miley, G. K. 1996, ApJS, 107, 621
de Vries, W. H., O'Dea, C. P., Baum, S. A., & Barthel, P. D. 1999, ApJ, 526, 27
de Vries, W. H., et al. 1997, ApJS, 110, 191
Dunlop, J. S., & Peacock, J. A. 1993, MNRAS, 263, 936
Fanaroff, B. L., & Riley, J. M. 1974, MNRAS, 167, 31P
Inskip, K. J., Best, P. N., Longair, M. S., & Röttgering, H. J. A. 2005, MNRAS, 359, 1393
Inskip, K. J., Best, P. N., Rawlings, S., Longair, M. S., Cotter, G., Röttgering, H. J. A., & Eales, S. 2002a, MNRAS, 337, 1381
Inskip, K. J., Best, P. N., Röttgering, H. J. A., Rawlings, S., Cotter, G., & Longair, M. S. 2002b, MNRAS, 337, 1407
Jackson, N., Sparks, W. B., Miley, G. K., & Macchetto, F. 1995, A&A, 296, 339
Koski, A. T. 1978, ApJ, 223, 56
Labiano, A., et al. 2005, A&A, 436, 493
Leahy, J. P., Pooley, G. G., & Riley, J. M. 1986, MNRAS, 222, 753
Lister, M. L., & Homan, D. C. 2005, AJ, 130, 1389
Ludke, E., Garrington, S. T., Spencer, R. E., Akujor, C. E., Muxlow, T. W. B., Sanghera, H. S., & Fanti, C. 1998, MNRAS, 299, 467
Mackay, C. D. 1969, MNRAS, 145, 31
Martel, A. R., et al. 1998, BAAS, 30, 890
Martel, A. R., et al. 1999, ApJS, 122, 81
McCarthy, P. J. 1993, ARA&A, 31, 639
McCarthy, P. J., Miley, G. K., de Koff, S., Baum, S. A., Sparks, W. B., Golombek, D., Biretta, J., & Macchetto, F. 1997, ApJS, 112, 415
McCarthy, P. J., Spinrad, H., & van Breugel, W. 1995, ApJS, 99, 27
McCarthy, P. J., & van Breugel, W. 1989, in Proc. NATO Advanced Research Workshop 264, The Epoch of Galaxy Formation, ed. C. S. Frenk (Dordrecht: Kluwer), 57
McCarthy, P. J., van Breugel, W., Spinrad, H., & Djorgovski, S. 1987, ApJ, 321, L29
Moy, E., & Rocca-Volmerange, B. 2002, A&A, 383, 46
Mullin, L. M., Hardcastle, M. J., & Riley, J. M. 2006, MNRAS, 372, 113
Neff, S. G., Roberts, L., & Hutchings, J. B. 1995, ApJS, 99, 349
Nilsson, K., Valtonen, M. J., Kotilainen, J., & Jaakkola, T. 1993, ApJ, 413, 453
O'Dea, C. P., et al. 2002, AJ, 123, 2333
Osterbrock, D. E. 1989, Astrophysics of Gaseous Nebulae and Active Galactic Nuclei (Mill Valley, CA: Univ. Science Books)
Perley, R. A. 1982, AJ, 87, 859
Price, R., Gower, A. C., Hutchings, J. B., Talon, S., Duncan, D., & Ross, G. 1993, ApJS, 86, 365
Rawlings, S., & Saunders, R. 1991, Nature, 349, 138
Reid, A., Shone, D. L., Akujor, C. E., Browne, I. W. A., Murphy, D. W., Pedelty, J., Rudnick, L., & Walsh, D, 1995, A&AS, 110, 213
Reuland, M., et al. 2003, ApJ, 592, 755
Rigler, M. A., Stockton, A., Lilly, S. J., Hammer, F., & Le Fevre, O. 1992, ApJ, 385, 61
Robinson, T. G., Tadhunter, C. N., Axon, D. J., & Robinson, A. 2000, MNRAS, 317, 922
Solórzano-Iñarrea, C., & Tadhunter, C. N. 2003, MNRAS, 340, 705
Swarup, G., Sinha, R. P., & Hilldrup, K. 1984, MNRAS, 208, 813
Tilak, A., O'Dea, C. P., Tadhunter, C., Wills, K., Morganti, R., Baum, S. A., Koekemoer, A. M., & Dallacasa, D. 2005, AJ, 130, 2513
Urry, C. M., & Padovani, P. 1995, PASP, 107, 803
van Ojik, R., Röttgering, H. J. A., Miley, G. K., & Hunstead, R. W. 1997, A&A, 317, 358
Véron-Cetty, M.-P., & Véron, P. 2003, A&A, 412, 399
Wright, E. L. 2006, PASP, 118, 1711